Telomerase Prevents Emphysema in Old Mice by Sustaining Subpopulations of Endothelial and AT2 Cells

Marielle Breau[1,2], Christelle Cayrou[1°], Dmitri Churikov[1°], Charles Fouillade[3], Sandra Curras-Alonso[4], Serge Bauwens[5], Frederic Jourquin[1], Laura Braud[1], Frederic Fiore[6], Rémy Castellano[7], Emmanuelle Josselin[7], Carlota Sánchez-Ferrer[8], Giovanna Giovinazzo[8], Eric Gilson[5], Ignacio Flores[8], Arturo Londono-Vallejo[4], Serge Adnot[2*], Vincent Géli[1* ≠].

[1]Marseille Cancer Research Centre (CRCM), U1068 INSERM, UMR7258 CNRS, UM105 Aix-Marseille University, Institut Paoli-Calmettes, Marseille, France. Ligue Nationale Contre le Cancer (Equipe labellisée).

[2] INSERM U955 and Département de Physiologie, Hôpital Henri Mondor, FHU SENEC, AP-HP, 94010, Créteil, FRANCE; and Université Paris-Est Créteil (UPEC), France.

[3] Institut Curie, Inserm U1021, CNRS UMR 3347, University Paris-Saclay, PSL Research University, Ortsay, France.

[4] Institut Curie, PSL Research University, CNRS UMR3244, Sorbonne Université, Telomeres and Cancer, 75005 Paris, France.

[5] Université Côte d'Azur, CNRS, Inserm, IRCAN, Faculty of Medicine Nice, France.

[6] Centre d'Immunophénomique, Aix Marseille Université, INSERM, CNRS UMR, Marseille, France.

[7] Marseille Cancer Research Centre (CRCM), TrGET Preclinical Platform, Institut Paoli-Calmettes, Inserm, CNRS, Aix Marseille Université, Marseille, France.

[8] Centro Nacional de Investigaciones Cardiovasculares Carlos III, 28029 Madrid, Spain. Centro de Biologia Molecular Severo Ochoa, CSIC-UAM, Cantoblanco, Madrid, Spain.

° Equal contribution

* Corresponding authors : serge.adnot@inserm.fr and vincent.geli@inserm.fr
≠ Lead contact : vincent.geli@inserm.fr

Keywords: Telomerase, telomere, senescence, lung, emphysema, aging, stem cell

Abstract
Accumulation of senescent cells has been causally linked to the development of age-related pathologies. Here, we characterized a new mouse model ($p21^{+/Tert}$) whose telomerase (TERT) is expressed from the p21 promoter that can be activated in response to telomere dysfunction. Lung parenchyma from $p21^{+/Tert}$ old mice accumulated fewer senescent cells with age and this correlated with a reduction in age-related alveolar space enlargement, a feature of pulmonary emphysema. This protection against emphysema depends on TERT catalytic activity and is associated with increased proliferation of pulmonary endothelial cells (EC) and capillary density. Single-cell RNA sequencing of lung cells revealed that TERT expression was associated with the enrichment of ECs expressing genes involved in vessel regeneration and in AT2 cells overexpressing airway epithelial cell and S/G2M markers. These findings indicate that p21-promoter-dependent expression of catalytically active telomerase prevents emphysema by sustaining the proliferation of subclasses of EC and AT2 cells.

Introduction
During aging, there is a progressive loss of organ and tissue function due to an impaired or reduced response to different insults that cannot be overcome by the intrinsic repair capacity of the affected organs (López-Otín et al., 2013). There is a growing consensus that accumulation of senescent cells in tissues that results from such insults represents a key process that contributes to age-related health decline(Campisi, 2013; Childs et al., 2015). During aging, cellular senescence induced in response to excessive telomere shortening, elicits a DNA damage response (DDR) leading to a permanent p53-dependent cell cycle arrest (d'Adda di Fagagna et al., 2003). In humans, an increasing number of age-related diseases have been associated with abnormally short telomeres including dyskeratosis congenita, aplastic anaemia, pulmonary fibrosis, and lung emphysema (Armanios and Blackburn, 2012).
Among the age-related diseases associated with abnormally short telomeres, lung diseases account for the most prevalent manifestations of mutant telomere genes (Barnes, 2016). Telomere erosion appears as a major risk factor for never smoker patients with pulmonary fibrosis while in smokers mutations that affect telomerase activity favour the development of emphysema/chronic obstructive pulmonary disease (COPD) (Alder et al., 2011, 2015; Armanios et al., 2007; Stanley et al., 2014). Moreover, lung specimens from patients with COPD were shown to accumulate senescent alveolar-epithelial cells, endothelial cells, and fibroblasts (Dagouassat et al., 2013).
In mouse, the regenerative capacity of lungs after irradiation is impaired in animals with short telomeres (Fouillade et al., 2020). Also, induction of DNA damage in mice with critically short or dysfunctional telomeres results in the development of pulmonary fibrosis (PF) (Povedano et al., 2015). Telomerase-deficient mice treated with cigarette smoke were shown to develop pulmonary emphysema due to the release of inflammatory cytokines by senescent cells (Alder et al., 2011; Amsellem et al., 2011). These results inspired development of adeno-associated vectors (AAV) encoding the telomerase reverse transcriptase gene (TERT) to assess the therapeutic effect of telomerase ectopic expression either in old mice or in mice with experimentally shortened telomeres (Bernardes de Jesus et al., 2012; Povedano et al., 2018a). Telomerase gene therapy had beneficial effects in delaying physiological aging and improving pulmonary function. However, the precise

mechanism by which TERT expression prevents lung damage or promotes lung endogenous repair remains to be elucidated.

The cyclin-dependent kinase inhibitor p21 is the main effector of p53, which is activated in response to DNA damage (El-Deiry, 2016) and telomere dysfunction (Smogorzewska and de Lange, 2002). In cellular models, p21 expression is regulated at the transcriptional level mainly by p53-dependent mechanisms (Engeland, 2018) but also by p53-independent signalling pathways (Gartel and Tyner, 1999; Karimian et al., 2016). The p53-dependent up-regulation of p21 leads to cell cycle arrest in the G1 phase and is the primary event inducing replicative senescence upon telomere shortening (Harper et al., 1995). Bioluminescence imaging of the p21 promoter activity in living mice revealed that it is active at a basal level in various organs and has a tendency to increased activity in the compartments where the cells exit proliferative state and differentiate (Ohtani et al., 2007; Tinkum et al., 2011). Importantly, p21 plays a role in the maintenance of stem cell quiescence (Cheng et al., 2000).

In this study, we generated and characterized a knock-in mouse model in which telomerase reverse transcriptase (TERT) is expressed from the $p21^{Cdkn1a}$ promoter (further on $p21^{+/Tert}$ mouse model). Since dysfunctional telomeres signal cell cycle arrest via the ATM-p53-p21 pathway (Herbig et al., 2004), the $p21^{+/Tert}$ model is expected to upregulate *Tert* expression in response to telomere dysfunction, thereby improving telomere maintenance. Using this unique fine-tuned regulatory loop allowing expression of telomerase specifically in cells with activated $p21^{Cdkn1a}$ we aimed at preventing their senescence. We uncovered that p21 promoter-dependent expression of TERT decreases the number of senescent cells in the lungs of old $p21^{+/Tert}$ mice and protects mice from age-associated emphysema. This protective effect relies on TERT catalytic activity and is associated with an increased of capillary density. Single-cell transcriptomics reveal that a subset of $p21^{+/Tert}$ lung ECs express genes promoting EC regeneration. Along the same line, a subset of $p21^{+/Tert}$ AT2 cells express genes that mark airway epithelial cells sustaining alveolar regeneration. These findings provide unique insights into the mechanism by which telomerase protects against age-related emphysema.

Results

Generation and validation of the $p21^{+/Tert}$ mouse model

To generate a mouse model that expresses TERT under control of the $p21^{Cdkn1a}$ promoter, we substituted the start codon of the *Cdkn1a* gene by a *mCherry-2A-Tert* cassette (Fig. 1A). The detailed construction of the targeting vector and integration of the mCherry-2A-mTert cassette in place of the start codon of Cdkn1a are shown in Fig. S1A-E (see Methods). The *mCherry-2A-Tert* allele retains regulatory 5' and 3'UTRs of the endogenous *Cdkn1a* gene. This *mCherry-2A-Tert* allele is transcribed into a polycistronic *mCherry-2A-Tert* mRNA which is translated into the two separate mCherry-2A and mTert polypeptides due to the ribosome skipping at the 2A sequence (Fig. 1A, Fig. S1F). Although the p21 coding sequence is present at the end of the polycistronic mRNA, it is not translated because *Tert* coding sequence ends with a stop codon. The generated $p21^{+/Tert}$ mouse therefore produces p21 protein from one allele and mCherry and Tert from the other allele. To demonstrate that TERT expressed from the *mCherry-2A-Tert* cassette is functional and can reconstitute active telomerase, we transfected $Tert^{-/-}$ ES cells with a plasmid carrying *mCherry-2A-Tert* under control of the constitutively active pCAG promoter and checked telomerase activity *in vitro*. Telomerase activity was readily detected in multiple transfected clones (Fig. 1B). As a validation of the conditional expression of the *mCherry-2A-Tert* cassette, we irradiated $p21^{+/+}$ and

$p21^{+/Tert}$ mice at the dose of 1.5Gy and checked the emission of the fluorescence by *in vivo* imaging. We observed an increase of emitted fluorescence after whole-body ionising radiation in the $p21^{+/Tert}$ mice after 24 and 48 hours (Fig. 1C). We next treated $p21^{+/+}$ and $p21^{+/Tert}$ littermates with intraperitoneal injection of doxorubicin, a DNA damaging drug known to promote p21 expression especially in the liver and kidneys (Ohtani et al., 2007). We observed increased levels of *mCherry-2A*-mTert transcripts in the liver and kidneys from $p21^{+/Tert}$ mice harvested 24 hours after doxorubicin treatment (Fig. S2A, B). Consistent with this result, mCherry fluorescence was increased in the same organs after doxorubicin treatment (Fig. S2C). In the same experiment, we also evaluated the level of p21 protein by semi-quantitative immunoblotting (Fig. S2C). $p21^{+/Tert}$ mice expressed about half of the amount of p21 protein compared to $p21^{+/+}$ in liver and kidneys pointing to the need of using use $p21^{+/-}$ controls in subsequent experiments.
Collectively, these results demonstrate that the *mCherry-2A-Tert* cassette produces active telomerase and is expressed under conditions known to induce the p53-dependent expression of p21.

p21-driven expression of telomerase in lungs reduces the age-related accumulation of senescent cells

To determine whether conditional expression of TERT could supress *in vivo* age-related cellular senescence in lungs, we monitored the number of lung parenchymal cells stained with senescence associated β-galactosidase activity at pH 6 (SA-β-Gal) in young (4-month-old) and old (18-month-old) mice from the 3 genotypes ($p21^{+/+}$, $p21^{+/-}$, and $p21^{+/Tert}$). Young mice from all genotypes exhibited a very low percentage of SA-β-Gal positive cells, with an overall mean for all three genotypes of 1.001% (±0.15). Lung cells from $p21^{+/+}$ and $p21^{+/-}$ old mice (18 months) displayed a significant increase in the percentage of SA-β-Gal positive cells albeit this number remained low while in the $p21^{+/Tert}$ mice, the percentage of SA-β-Gal positive cells did not increase with age (Fig. 2A). The same cohort of mice was then used to examine the number of $p16^{INK4a}$-positive lung cells and we distinguished vascular and alveolar cells, based on histological morphology. Consistent with the results above, young mice from the 3 genotypes exhibited a very low number of vascular and alveolar cells stained for p16. Lung cells from $p21^{+/+}$ and $p21^{+/-}$ old mice displayed a significant increase in the number of p16-positive cells amongst vascular cells (Fig 2B) even if the number of these cells remained below 10 %. The percentage of alveolar cells expressing p16 also significantly increased in old $p21^{+/+}$ when compared to young $p21^{+/+}$ mice, although this increase did not reach significance in old $p21^{+/-}$. Strikingly, the percentage of p16-positive cells amongst vascular and alveolar cells remained very low in old $p21^{+/Tert}$ mice (Fig. 2B), thus suggesting that expression of TERT under the control of p21 markedly reduces the number of senescent cells in both compartments. Consistent with this interpretation, we found that p16 and SA-β-Gal positive lung cells were positively correlated in $p21^{+/+}$ and $p21^{+/-}$ cells but not in $p21^{+/Tert}$ mice (Fig. 2C). We also counted the number of p21-positive cells both in alveolar and in vascular cells (Fig. 2D). In all genotypes, we detected a mild increase in the number p21-positive alveolar cells in old mice when compared to young mice, although this increase was only significant in the $p21^{+/+}$ background (Fig. 2D). The prevalence of p21 expression in vascular cells was higher than in alveolar cells and this increase was observed with age, albeit it did not reach significance in any of the genetic backgrounds

(Fig. 2D). Overall, we conclude that the p21 promoter-driven expression of TERT reduced the global number of cells either expressing p16 or positive for SA-β-gal, two robust markers of senescent cells.

Senescence correlates with the fraction of very short telomeres

We further investigated whether the decrease of cellular senescence was associated with a global decrease of DNA damage and telomere induced foci (TIF) in lung parenchyma cells. Indeed, telomere damage has been reported to increase in patients with COPD and during murine lung aging (Birch et al., 2015). We performed immunofluorescence staining against γH2AX together with telomere specific FISH in lungs from old $p21^{+/Tert}$ mice. Analysis revealed a modest but not significant decrease in the percentage of parenchyma lung cells with γH2AX foci in the $p21^{+/Tert}$ mice compared to $p21^{+/+}$ (Fig. 3A, B). We were also not able to detect a difference between $p21^{+/+}$ and $p21^{+/Tert}$ mice in the percentage of lung cells exhibiting TIFs (Fig. 3A, B). However, it is likely that the minor fraction of short telomeres that reflects damaged telomeres could escape the detection by the telomeric probe in the FISH experiment. We thus investigated the presence of very short telomeres (VST) in lungs from six $p21^{+/+}$ and six $p21^{+/Tert}$ old mice compared to young counterparts by using the TeSLA method that allows measuring the distribution of the shortest telomeres in cells and tissues (Lai et al., 2017) (Fig. 3C and Fig. S3). Quantification of the results (See Methods) indicated that the fraction of short telomeres was not significantly different in between $p21^{+/+}$ and $p21^{+/Tert}$ mice (Fig. 3C). However, the cumulative number of VST telomeres in lung cells from $p21^{+/+}$ mice was highly correlated with the number of cells endowed with SA-β-Gal activity. This correlation was also observed at a lower level in $p21^{+/Tert}$ mice suggesting that the fraction of very short telomeres is a marker of senescence in mice (that are otherwise $TERT^{+/+}$) (Fig. 3D).

Smooth muscle cells from $p21^{+/Tert}$ pulmonary arteries bypass senescence ex-vivo

To deeply characterize the p21-promoter dependent expression of TERT on cellular senescence, we sought to test ex-vivo its effect on the proliferation of cultured pulmonary artery smooth muscle cells (PA-SMCs) isolated from lungs of young mice. PA-SMCs of the three genotypes: $p21^{+/+}$, $p21^{+/Tert}$ (littermate) and $p21^{+/-}$ were cultured in standard conditions (20% oxygen) (Fig. 4A). Under these conditions we expect TERT to be induced in most of the cells because of the oxidative stress created by the culture conditions (Fig. 4B). Cells from $p21^{+/+}$ and $p21^{+/-}$ mice entered into senescence after a few passages, with a final mean population doubling level (PDL) of 15,51 (+/- 4,14) and 36,09 (+/- 8,30) respectively. PA-SMCs cultured at the same time from $p21^{+/Tert}$ mice never entered into senescence and proliferated with a much faster rate (Fig. 4A). The difference in cumulative PDL between $p21^{+/Tert}$ and both $p21^{+/+}$ and $p21^{+/-}$ became significant at passage 7. When all $p21^{+/+}$ and $p21^{+/-}$ cells stopped proliferating, the mean PDL for $p21^{+/Tert}$ cells was 63,52 (+/- 9,11), and these cells were still proliferating (Fig. 4A). We confirmed induction of the mCherry-2A-Tert mRNA expression in the cultured $p21^{+/Tert}$ cells by qRT-PCR (Fig. 4C), and also detected a slight increase of telomerase activity at early passages, before PA-SMCs cumulative PDL curve became significantly different (Fig. 4D). Since proliferation arrest of cultured mouse cells has been reported to stem from oxidative stress rather than from telomere shortening (Parrinello et al., 2003), our results may appear surprising. Nevertheless, it is formally possible that oxidative damage also occurs at telomeres thus resulting in stalled replication forks that generate very short telomeres, which could be repaired by telomerase (Matmati et al., 2020). We measured the load of VSTs in wild-type cells and $p21^{+/Tert}$ PA-SMCs by using the TeSLA technique. While the cumulative number of short telomeres increased

with passages in $p21^{+/+}$ PA-SMCs, the load of short telomeres was identical at passages 4 and 10 in $p21^{+/Tert}$ PA-SMCs (Fig. 4E). Therefore, proliferation of the cultured $p21^{+/Tert}$ PA-SMCs coincides with conditional expression of TERT and reduced prevalence of the VSTs.
Another possible explanation of the proliferative capacity of the $p21^{+/Tert}$ cells is that elevated TERT expression somehow reduces the level of DNA damage that may occur in these cells in particular at telomeres (Fouquerel et al., 2019). Thus, we analysed the occurrence of the γH2AX foci in the nuclei of the cultured cells of all three genotypes ($p21^{+/+}$, $p21^{+/-}$, and $p21^{+/Tert}$). Quantification of the γH2AX foci showed that $p21^{+/Tert}$ cells harboured the largest number of γH2AX per nucleus among the three genotypes (Fig. S4) indicating that TERT expression in cultured cells does not decrease, but instead rather increase the global level of DNA damage likely as a result of their higher proliferation rate. We could not determine the occurrence of TIFs since γH2AX foci rarely co-localized with telomere FISH signal. Despite the higher load of DNA damage, $p21^{+/Tert}$ PA-SMCs continued to proliferate indicating that they did not establish a robust DDR.

Conditional expression of telomerase protects against age-related emphysema

We next sought to determine the impact of the conditional expression of telomerase on age-related manifestations in the lung, such as emphysema as it has been widely documented in old C57Bl6 mice (Huang et al., 2007). Previous studies have revealed mechanistic links between p16 expression and the occurrence of emphysema (Kim et al., 2019). Emphysema is characterized by lung airspace enlargement as a consequence of a decrease of lung elasticity with advanced age (Sharma and Goodwin, 2006). We performed histological analyses of the airspace morphology in $p21^{+/+}$, $p21^{+/-}$, and $p21^{+/Tert}$ young and old mice as previously described (Dunnill, 1962). Morphometry studies did not reveal air space enlargement in young mice from the three genotypes (Fig. 5A). As expected, old $p21^{+/+}$ and $p21^{+/-}$ mice developed emphysema as defined by an increase in mean-linear intercept (MLI) length reflecting increased alveolar size. In contrast, old $p21^{+/Tert}$ mice did not exhibit air space enlargement (Fig. 5A). These data indicated that the p21-dependent expression of TERT protected mice from age-related emphysema.
We also measured bronchiolar thickness and sought for manifestations related to lung fibrosis in the same cohort of mice. Bronchiolar thickness has been demonstrated to decrease with age (Michaudel et al., 2018; Watson et al., 2020) while it increases in response to cigarette smoke (Shu et al., 2017). It is also known that collagen deposition in the lung increases with age (Hübner et al., 2008). These analyses did not reveal significant variation of bronchiolar wall thickness with age or between genotypes (Fig. 5B). In contrast, we observed a discreet but significant increase of the Ashcroft score (a morphological test for pulmonary fibrosis) in lungs from $p21^{+/+}$ and $p21^{+/-}$ mice with age, but not in $p21^{+/Tert}$ mice (Fig. 5C), indicating a minimal alveolar fibrous thickening in $p21^{+/+}$ and $p21^{+/-}$ mice with age. Taken together, these results indicate that p21-dependent expression of TERT protects mice from age-related emphysema and morphological changes of the lung.

Suppression of emphysema in $p21^{+/Tert}$ lungs is associated with endothelial cell proliferation and capillary density

Although lung emphysema pathogenesis is not yet fully understood, it is now accepted that the vascular compartment has a major role in the pathophysiology of this disease, like in most lung diseases (Voelkel et al., 2011). Because $p21^{+/Tert}$ mice are protected against senescent cells accumulation and emphysema, we sought to determine whether this protection was associated to

higher levels of cellular proliferation, which could then favour cell renewal and preserve tissue architecture with age. We thus assessed cell proliferation in the lungs of old mice (18 months) from the three genotypes by performing intraperitoneal injection of bromodeoxyuridine (BrdU) followed by analysis of BrdU incorporation. We found a higher cell proliferation level in $p21^{+/Tert}$ mice compared to control mice, and this finding was associated to a significantly lower MLI in the same mice (Fig. 6A, B). BrdU positive cells were mainly observed in the vascular compartment (Fig. 6A, middle panel). The extent of emphysema suppression was correlated with the number of BrdU positive cells (Fig. 6C). We also quantified the number of SA-β-Gal positive cells. As above, we found that the number of senescence cells was reduced in $p21^{+/Tert}$ lungs (Fig. 6D).
Since most BrdU-positive cells were found in the vascular compartment, we wondered if this enhanced proliferation capacity was associated with a preserved vasculature in $p21^{+/Tert}$ mice. We thus measured capillary density by anti-isolectin B4 immunofluorescence (Kobayashi et al., 2018)(Kobayashi et al., 2018). The results indicate a strong tendency for increased capillary density with age in the p21+/Tert (Fig. 6E). These results suggest that TERT, when under the control of p21 promoter, promotes endothelial cell proliferation with age thus preserving capillary density, which provides a potential explanation for its protective role against emphysema in old mice.

Protection against age-related emphysema requires the catalytic activity of TERT

The canonical role of telomerase is to elongate telomeres and extend cellular proliferation capacity. To determine whether the catalytic activity of telomerase was required for lung protection, we created a new mouse line (called $p21^{+/Tert\text{-}CI}$) based on $p21^{+/Tert}$ mice, but carrying a point mutation (D702A) in the active site of TERT. We performed the experiments described above (MLI, cellular senescence, cell proliferation and capillary density) in $p21^{+/Tert}$ and $p21^{+/Tert\text{-}CI}$ mice at the age of 18 month. While values for $p21^{+/Tert}$ were comparable to those obtain in previous experiments, we found that, in comparison, $p21^{+/Tert\text{-}CI}$ presented a significant increase in MLI (Fig. 7A), associated with an increase in both the number of vascular and alveolar p16-positive cells (Fig. 7B) and SA-β-Gal staining (Fig. 7C). $p21^{+/Tert\text{-}CI}$ mice also presented an increase in vascular p21-positive cells, albeit not in alveoli (Fig. 7D). These observations are in agreement with observations in vitro showing that catalytically inactivated telomerase does not protect against cellular senescence. We also observed a very low level of proliferative cells in $p21^{+/Tert\text{-}CI}$ mice lungs compared to $p21^{+/Tert}$ mice (Fig. 7E), a level comparable to that observed in age-matched $p21^{+/+}$ and $p21^{+/-}$ mice lungs (Fig. 6B). Finally, capillary density in $p21^{+/Tert\text{-}CI}$ mice was also comparable to that detected in $p21^{+/+}$ and $p21^{+/-}$ mice, and significantly decreased with respect to $p21^{+/Tert}$ mice (Fig. 7F). Overall, $p21^{+/Tert\text{-}CI}$ mice exhibit the same aging characteristics in the lung as control mice indicating that inactivation of TERT enzymatic activity abolishes the protection conferred by the p21-promoter dependent expression of TERT. These results strongly support the idea that TERT acts either by elongating critically short or damaged telomeres (Birch et al., 2015; Fouquerel et al., 2019; Matmati et al., 2020).

A subcluster of $p21^{+/Tert}$ gCap cells express markers associated with regeneration

To further understand how ectopic expression of telomerase driven by the p21 promoter could suppress emphysema in old mice, we performed single-cell transcriptomics on lung cells from 18 month-old $p21^{+/+}$, $p21^{+/Tert}$ and $p21^{+/-}$ mice. Single-cell suspensions from whole lungs were prepared and loaded onto a 10x Genomics Chromium system. For a single lung, around 5000 individual lung cells were encapsulated and libraries were prepared and sequenced. Unique molecular identifiers

(UMI), number of genes detected per cell, and reads aligned to the mouse genome reference were similar for the three mice. We performed dimensionality reduction and unsupervised cell clustering to identify distinct cell types based on shared and unique patterns of gene expression (see Methods). For each mouse, clustering of gene expression matrices identified cell types that were in good agreement with the published Mouse Cell Atlas (MCA) (Han et al., 2018) (Fig. S5A, Table 1). Cell-type classes of immune and non-immune cells were similar for the 3 mice (Fig. S5A, B). We monitored p21 expression in each cell type class. In immune lung cells, Cdkn1a (p21) was mainly expressed in interstitial and alveolar macrophages, monocytes, and in dendritic cells while in resident lung cells, it was mainly expressed in endothelial cells (Fig. S5C). Of note, we cannot directly detect the transgene (mcherry-2A-Tert) transcript because the 10x Genomics single-cell 3′ chemistry only provides sequence information on the region flanking the polyA-tail.

Because pulmonary endothelial cells (EC) seem to play a key role in the development of emphysema, we first targeted our single-cell transcriptomics analysis to EC, many of which expressed p21 (Fig. S5C). We annotated lung EC to specific vascular compartment based on recently published markers of lung EC (Kalucka et al., 2020) (Fig. S6). We identified 5 classes of EC comprising 2 capillary classes, 1 artery, 1 vein, and 1 lymphatic class (Fig. 8A, B) (Table 2). Interestingly, capillary class 1 and 2 were recently identified as aerocytes (aCap) involved in gas exchange and trafficking of leucocytes and as general capillary cells (gCap) that function in vasomotor tone regulation and in capillary homeostasis (Gillich et al., 2020). We reasoned that p21-expression should reflect Tert expression in $p21^{+/Tert}$ cells (but not in WT and in $p21^{+/-}$) since both genes belong to the same polycistronic mRNA. For each mouse ($p21^{+/+}$, $p21^{+/-}$, $p21^{+/Tert}$), we therefore decided to compare differentially expressed genes (DEG) between p21-positive and -negative EC. We uncover that a number of genes were significantly overexpressed specifically in p21-positive cells in $p21^{+/Tert}$ EC (Fig. 8C) Strikingly, most of these genes are functionally related (Fig. 8D) and are positively regulated by the stress response gene Atf3 (Cyclic AMP-dependent transcription factor 3) involved in EC regeneration (McDonald et al., 2018) (See discussion). Individual expression of DEG between p21-positive and -negative EC in the five classes of EC is shown in Figure S7.

Because, old $p21^{+/Tert}$ mice had an increased lung capillary density, we focussed our attention to capillary class 2 cells (gCap) that are involved in capillary homeostasis (Gillich et al., 2020). We uncover that many genes overexpressed in p21-positive (versus –negative) EC were also significantly expressed in $p21^{+/Tert}$ gCaps (Figure S7). For the 3 mice, we performed Pearson correlations to analyse co-expression in gCaps of the genes up-regulated in p21-positive cells (Fig. 8E). Remarkably, we found that the functionally related genes (FRG) (Btg2, Fosb, Fos, Junb, Jund, Ier2, Ier3, Egr1, Zfp36, Socs3, Jun, Klf4, Klf2) were significantly co-expressed in $p21^{+/Tert}$ gCaps suggesting that these genes could be directly or indirectly co-regulated by Tert.

We further uncover that gCaps could be subclustered in two clusters named 1 and 2 (Fig. 8F). Of note, cluster 2 was overrepresented in $p21^{+/Tert}$ gCaps raising the possibility that the differences in gene expression could be related to the increased number of cells belonging to cluster 2 (Fig. 8G). Moreover, we found that most FRG that we defined above were mainly overexpressed in p21-positive cluster 2 cells in comparison to cluster 1 cells (Fig. 8H).

Collectively, these results suggest that TERT sustain the growth of a subpopulation of gCap cells (cluster 2) expressing markers associated with EC regeneration (see discussion).

A subclass of $p21^{+/Tert}$ AT2 cells express markers of club cells and S/G2M associated genes

Because Tert targeting in AT2 cells was previously shown to prevent pulmonary fibrosis progression (Povedano et al., 2018b), we next clustered $p21^{+/+}$, $p21^{+/-}$, and $p21^{+/Tert}$ AT2 cells resulting in a detailed map of AT2 cells for each genotype. Two-dimensional representations revealed 3 main clusters within AT2 cells whose proportion differed for the three mice (Fig. 9A). Cluster 1 was found in all three mice, with an over-representation in WT mice. Cluster 2 was strictly specific for $p21^{+/-}$ and $p21^{+/Tert}$ mice while cluster 3 was over-represented in $p21^{+/Tert}$ mice. These results suggest that p21 haploinsufficiency would favour the generation of cluster 2 cells while p21-promoter driven expression of TERT in lung promotes the expansion of cluster 3.
We analysed DEGs in all AT2 cells in between the $p21^{+/+}$, $p21^{+/-}$, and $p21^{+/Tert}$. A large number of genes were differentially expressed in $p21^{+/Tert}$ AT2 cells compared to either $p21^{+/+}$ or $p21^{+/-}$ (Table 3). However, a number of these genes were also differentially expressed in between $p21^{+/-}$ and $p21^{+/+}$ likely reflecting differences in cell clusters in between the three mice. We selected genes whose differential expression were much more significant in between $p21^{+/Tert}$ and $p21^{+/+}$ than in between $p21^{+/-}$ and $p21^{+/+}$ (Fig. 9B and Fig. S8). Hierarchical clustering of genes allowed the identification of 4 groups of genes that were up-regulated in $p21^{+/Tert}$ AT2 cells (Fig. 9B and 9C). The first group of genes was mainly overexpressed in AT2 cluster 3 whose number of cells was increased in $p21^{+/Tert}$. This group was characterized by the expression of the club cell markers Scgb1a1 (Secretoglobin family 1A member 1), Fth1 (Ferritin heavy chain) and Hp (Haptoglobin), as well by the lack of Cdkn1a expression (Fig. 9B). Genes from group 2 and 3 were mainly overexpressed in AT2 cluster 2 and to a lesser extend in AT2 cluster 3. We could identify in group 3 a signature of functionally related genes containing MHC class 1 genes (H2-D1, H2-K1, H2-Q7, B2m) and Scd1 (Acyl-CoA desaturase) (see discussion). The fourth group of genes was overexpressed in AT2 class 1 and 2. It includes Wdfy1, a positive regulator of the TLR3/4 signalling pathway, Cd59a, an inhibitor of the complement membrane attack complex), and IL6 whose expression was absent in AT2 class3. Interestingly, we next uncovered that a higher number of cells belonging to cluster 3 cells (compared to cluster 1 and 2 cells) expressed genes associated with the S/G2M phase when compared to cluster 1 and 2, which mainly expressed G1-phase genes (Fig. 9D), suggesting that cluster 3 may support AT2 cell regeneration.
Many more genes were significantly down-regulated in $p21^{+/Tert}$ AT2 cells compared to $p21^{+/+}$ or $p21^{+/-}$ likely reflecting differences in the distribution of the AT2 cell classes in $p21^{+/Tert}$ compared to $p21^{+/+}$ and $p21^{+/-}$ (Fig. S8). Many of them are related to metabolic processes. For instance, down-regulated genes include mitochondrially-encoded subunits of the respiratory chain (mt-Nd3, mt-Nd5, mt-Atp8 and mt-Co1), a number translation factors (Eif3l, Eif3m, Eif3e, Eif4b, Eif2s3y, Eef2), and several E3 ubiquitin ligases (Rnf4, Pja2, Sh3rf1, Arih2, Siah1a, Nedd4).

In summary, $p21^{+/Tert}$ AT2 cells are enriched in a subclass of AT2 cells (cluster 3) that are characterized by markers of club cells and expression of S/G2M genes. On the other hand, p21 haploinsufficiency may promote the generation of cluster 2 cells. These results suggest that p21-dependent Tert expression and p21 haploinsufficiency both promote the mobilization of specific populations that share features with cells involved in the repair of alveolar epithelia after lung injury (see discussion).

Discussion

Emphysema and chronic bronchitis are the two manifestations of COPD, which is considered as a disease of accelerated aging of the lungs (Mercado et al., 2015). Specifically, emphysema is characterized by alveolar airspace enlargement and loss of elasticity, associated with senescence of alveolar and endothelial cells (Boyer et al., 2014; Breau et al.; Tsuji et al., 2010). Numerous studies have shown that abnormally short telomeres and senescent cell accumulation are found in the lungs of COPD patients suggesting a direct relationship between short telomeres, senescence and the development of the disease (Alder et al., 2011; Houben et al., 2009; Savale et al., 2009; Stanley et al., 2014; Tsuji et al., 2010). These conclusions have been strengthened by mouse studies showing that alveolar stem cell failure is a driver of telomere-mediated lung disease (Alder et al., 2015). Collectively these results suggest that DNA damage, cellular senescence, stem cell exhaustion, and likely mitochondrial dysfunction, all induced by accumulation of short telomeres, contribute together to lung injury. Because TERT may reverse these processes, TERT-based gene therapy (Martínez and Blasco, 2017) may be clinically beneficial to treat COPD. However, the mechanism by which *in vivo* telomerase expression could prevent the occurrence of emphysema during aging remains to be elucidated. More generally, many questions remain unanswered as to the impact of telomerase on regeneration *in vivo*.

In this study, we designed a fine-tuned regulatory loop allowing the conditional expression of telomerase under conditions that induce the expression of p21, including the accumulation of critically short telomeres. Importantly this conditional expression of TERT has been introduced in telomerase-positive mice ($Tert^{+/+}$), e.g. with long telomeres. Theoretically, the exogenous TERT will be expressed *in vivo* in the subset of cells carrying critically short telomeres and about to enter senescence because of p53 activation. Although p21 expression is not exclusively dependent of p53, the $p21^{+/Tert}$ mouse provides a unique tool allowing us to evaluate the impact of TERT re-expression on age-related diseases.

We exploited the fact that C57BL/6NRj mice naturally develop age-related emphysema to test *in vivo* the effects of TERT expression under the control of the p21 promoter. We report that the p21 promoter-driven expression of TERT in old lungs reduces the number of cells expressing robust markers of senescence such as p16 and β-gal. This is not due to the haploinsufficiency of p21 since the reduction of senescent cells was not observed in $p21^{+/-}$ mice, although we cannot completely exclude a role of the reduced level of p21 in the phenotypes of the $p21^{+/Tert}$ mouse. In old mice, we were able to correlate the presence of very short telomeres (<400 bp) in lung cells with cellular senescence. Explanted PA-SMCs from $p21^{+/Tert}$ mice grown *in vitro* escaped senescence and showed a reduced number of very short telomeres which correlated to an increase of telomerase activity. *In vivo*, though, telomerase activity remained barely detectable (Fig. S9) likely reflecting the low number of cells expressing Tert. Nevertheless, $p21^{+/Tert}$ mice were protected from age-related emphysema and mild fibrous alveolar thickening naturally occurring in $p21^{+/+}$ and $p21^{+/-}$ old mice. The decrease in the number of senescence cells and of cells with global DNA damage (γH2AX-positive cells) in lungs of $p21^{+/Tert}$ mice correlated with the extent in the reduction of age-related emphysema. However, we were unable to determine whether the reduced DNA damage observed *in vivo* in the $p21^{+/Tert}$ lung parenchyma was associated with a reduction of DNA damage at telomeres. Indeed, it has been previously reported that the DNA damage response at telomeres was contributing to lung aging and COPD (Birch et al., 2015).

Remarkably, we further uncovered that old p21$^{+/Tert}$ mice exhibited an increased proliferation of cells compared to control mice. In agreement with this observation, capillary density was increased in p21$^{+/Tert}$ mice indicating that p21-promoter dependent expression of TERT during aging improves capillary vasculature maintenance. These results suggest that TERT could prevent age-related emphysema by promoting microvasculature. This hypothesis is supported by previous studies showing a link between vascular density, endothelial cells and emphysema (Cordasco et al., 1968; Kasahara et al., 2000, 2001). Overall, these results suggest that TERT-stimulated proliferation of vascular cells sustains pulmonary function in aging mice.

The single-cell experiments provide a theoretical framework that potentially explains how telomerase expression promotes capillary density in old mice. We discover that p21-positive p21$^{+/Tert}$ EC express a signature of functionally related genes (Fos, Junb, Fosb, Nfkbiz, Jund, Dusp1, Jun, Rhob, Egr3, Btg2 Egr1, Zfp36, Ier2, Ier3, Ier5, Klf2, Klf4, Socs3, Icam1, Irf1), many of them being positively regulated by Atf3, an important transcriptional regulator required for regeneration of the endothelial lining of large arteries following injury (McDonald et al., 2018). We further report that a subpopulation of gCap cells was overrepresented in p21$^{+/Tert}$ gCap cells and preferentially expressed the p21$^{+/Tert}$ specific signature of FRG. The single cell analysis indicates that overexpression of these functionally related genes is partly due to the over-representation of cluster 2 cells in p21$^{+/Tert}$ gCap cells but also to the higher level of expression of these genes in cluster 2 cells. These results suggest that stress response genes related to Atf3 that contribute to repair large vessel injury (McDonald et al., 2018), may also promote an increase of capillary density.

Among these FRGs, we found AP-1 factors (Fos, Fosb, Jun, JunB, JunD) that are involved in numerous cellular functions such as proliferation, survival, transformation, and protection against oxidative stress (Breau et al.; Reddy and Mossman, 2002). FRG also include the transcription factor Egr1 that was shown to play an important role in the formation of new blood vessels from the pre-existing vasculature (Khachigian et al., 1996), and Klf2 (Krüppel-like factor 2) that regulates endothelial gene expression in response to shear stress due to flow (Hergenreider et al., 2012). Interestingly, Klf4 was shown to recruit β-Catenin to the promoter of *Tert* to promote telomerase expression in mouse embryonic stem cells (Hoffmeyer et al., 2012). The FRG also include a number of genes attenuating inflammation. Nfkbiz inhibits the DNA binding activity of p65 and p50 NF-kb subunits (Taniguchi and Karin, 2018; Totzke et al., 2006) while Zfp36 was shown to reduced inflammation in aortic EC by inhibiting Nf-kb transcriptional activation and by binding to cytokine mRNAs (Schichl et al., 2009; Zhang et al., 2013). On their side, Socs3 (Suppressor of cytokine signalling 3) negatively feedbacks cytokines through the JAK/STAT pathway (Carow and Rottenberg, 2014) while Dusp1 (Dual-Specificity Phosphatase 1) plays a central role in the resolution of inflammation (Hoppstädter and Ammit, 2019).

We propose from these results that gCap cluster 2 cells by expressing a specific signature associated with EC regeneration could account for the increase capillary density that we observed in p21$^{+/Tert}$ mice and therefore contribute to the suppression of emphysema in p21$^{+/Tert}$ mice.

We also focussed our single-cell studies to Type II alveolar cells since their dysfunction has been linked to lung disease (Parimon et al., 2020; Ranchoux et al., 2018). We uncover that p21$^{+/Tert}$ AT2 cells were enriched in a specific subpopulation that was present in p21$^{+/-}$ but absent in WT. This subpopulation expressed several markers of club cells and was characterized by the lack of expression of Cdkn1a. Remarkably, these cells exhibited a higher number of dividing cells. These results therefore raise the possibility that telomerase expression may promote the mobilization of a

source of club cells that differentiates into AT2 cells while retaining markers of the original lineage. This cluster 3 of AT2 cells shares features with cells involved in the repair of alveolar epithelia after lung injury (Spella et al., 2019; Zheng et al., 2013) but are different from bronchioalveolar stem cell (BASC) (Kim et al., 2005; Liu et al., 2019; Salwig et al., 2019). Strikingly, cluster 2 and 3 cells (either in $p21^{+/-}$ or in $p21^{+/Tert}$) overexpressed MHC class I genes. These genes were reported to mark a minor subpopulation of club-like cells endowed with the ability to support alveolar regeneration in mice after bleomycin injury (Kathiriya et al., 2020). Because p21 plays a role in maintaining the quiescence state of stem cells (Cheng et al., 2000; Kippin et al., 2005), it is possible that p21 haploinsufficiency favours the mobilization of this subpopulation of club-like cells that will further differentiate into AT2 cells. Interestingly, the four MHC class I genes H2-K1, H2-Q7, H2-D1, and B2m (whose high expression is usually associated with an interferon-gamma signature) together with Acyl-CoA desaturase 1 (Scd1) were reported to be overexpressed in AT2 cells from old mice compared to young mice (Angelidis et al., 2019).

Because TERT has extra-telomeric functions not related to its catalytic activity (Ségal-Bendirdjian and Geli, 2019), we tested whether $p21^{+/Tert\text{-}CI}$ mice were also protected from emphysema. Our results indicated that $p21^{+/Tert\text{-}CI}$ mice developed emphysema with age associated with wild-type levels of vascular and alveolar p16-positive cells. Similarly, capillary density was not stimulated in $p21^{+/Tert\text{-}CI}$ mice in contrast to what happened in $p21^{+/Tert}$. Therefore, inactivation of telomerase catalytic activity seemed to abolish the protection conferred by the $p21^{+/Tert}$ cassette pointing out the crucial role of TERT canonical activity in sustaining lung function. These results support studies indicating that short telomeres are important for the predisposition to lung disease in patients with mutations affecting telomere elongation by telomerase (Stanley et al., 2014). Our results support a model in which mice accumulate with age a subset of presenescent cells with critically short/damaged telomeres that are not yet engaged into an irreversible senescence process. The conditional expression of TERT by elongating/repairing the very short telomeres may prevent these cells to initiate a DNA damage response and to become senescent. This process would be particularly important in maintaining the regenerative capacities of stem/progenitor cells involved in sustaining the alveolar function as discussed above and as proposed by ex-vivo experiments by (Alder et al., 2011). Overall, our results shield new light for the development of TERT-AAV9 treatments to treat lung diseases (Povedano et al., 2018b).

Acknowledgments

We are grateful to the CRCM animal facility for taking care of the mouse strain colonies. We thank Lea Harrington for providing mTert-/- mouse ES cells. CIPHE is supported by PHENOMIN (French National Infrastructure for mouse Phenogenomics; ANR10-INBS-07). The imaging studies carried out on the TrGET platform (IPC/CRCM) received financial support from ITMO Cancer as part of the 3rd Cancer Plan for the acquisition of dedicated equipment. Work in VG's Lab is supported by "La Ligue Contre le Cancer", équipe labellisée, La Région SUD (Volet Général), and the "Institut National du Cancer" (INCA), PLBIO 2019 and the cross-cutting Inserm program on aging (AgeMed). SA's Lab is supported by grants from the INSERM, Ministère de la Recherche, *Agence Nationale pour la Recherche* (ANR), *Institut National du Cancer* (INCA), *Fondation pour la Recherche sur la Cancer* (ARC) and *Fondation pour la Recherche Médicale* (FRM). ALV's lab is supported by grants from ANR (Lustra), INCa (PLBIO2019), EDF (CT9818) and La Ligue contre le

cancer-Paris (RS21/75-24). SCA is a recipient of a European CO-FUND PhD fellowship from Institut Curie. IF's lab was funded by grants from the Spanish Ministry of Science and Innovation (PID2019-110339RB-I00) and the Comunidad de Madrid (S2017/BMD-3875). EG's lab was supported by the Fondation ARC (Program ARC), the ANR grants TELOPOST and the cross-cutting Inserm program on aging (AgeMed). This work was performed using the PICMI facility of IRCAN (supported by FEDER, ARC, le Ministère de l'Enseignement Supérieur, la région Provence Alpes-Côte d'Azur and Inserm).

Author contributions

Conceptualization, M.B., S.A., A.L.V., I.F. and V.G; Methodology, M.B., D.C., C.C., C.F., S.C.A., S.B., F.J., L.B., F.F., R.C., E.J., C.S.F., G.G.; Investigation and validation, M.B., D.C., C.C., C. F., E. G., A. L. V., S. A., V.G.; Supervision, M.B., A.L.V, S.A., V.G, Project administration, A.L.V., S.A., V.G.; Funding acquisition, E.G., A.L.V., S.A., V.G, Writing-original draft, VG; Writing Review-Editing, M.B., C.C., D.C., A.L.V., S.A.

Declaration of interests

The authors declare no competing interests

FIGURE LEGENDS

Figure 1. Construction and validation of the p21$^{+/Tert}$ mouse model.

(A) Schematic of the modified *Cdkn1a* locus, the mRNAs transcribed, and the proteins translated. The *mCherry-2A-Tert* cassette was inserted in place the start codon of Cdkn1a (see Figure S1 for details). The gene locus is drawn to scale with intron 1 contracted. The 2A peptide sequence causes a "ribosomal skip" that generates two independent polypeptides, mCherry and TERT, from the knock-in (KI) allele.

(**B**) Tert$^{-/-}$ ES cells re-gain telomerase activity after transfection with the plasmid carrying mCherry-2A-Tert cassette (See Methods). *In vitro* telomerase activity was assayed using by the Telomere Repeat Amplification Protocol (TRAP). The 6 bp ladder reflects telomerase activity. The arrow indicates the internal standard control (IC). IPSC and ES Tert$^{-/-}$ cells were used as positive and negative controls, respectively.

(**C**) mCherry imaging *in vivo* after whole-body ionising radiation of 1.5 gray. The fluorescence emitted by the mCherry was followed post-irradiation at the indicated times by *in vivo* mCherry imaging (Excitation = 545 nm, Background = 495 nm, Emission = 615 nm). The colour scale is indicated.

Figure 2. *p21$^{+/Tert}$ mice are protected against age-related associated senescent cells accumulation in the lung.*

(**A**) Upper panel: representative micrographs of SA-β-Gal staining in the lungs from p21$^{+/+}$, p21$^{+/-}$ and p21$^{+/Tert}$ young (4-month-old) and old (18 month) mice. Blue: positive cells, Red: nuclear counterstaining using neutral red. Lower panel: quantification of the percentage of cells positive for SA-β-Gal in each group.

(**B**). Upper panel: representative micrographs of mice lung immunohistochemistry against p16 (brown) with nuclear hemalum coloration (blue). Brown nucleus were considered positives. Lower left panels: Quantification of the percentage of vascular p16-positive cells. Vessels were identified according to their morphology. Lower right panel: p16-positive cells in lung tissue excluding vessels and bronchus.
(**C**) Correlation between the overall percentage of p16 and SA-β-Gal positive cells in lung from mice of the indicated genotypes. Each dot represents one individual mice.
(**D**) Upper panel: representative micrographs of mice lung immunohistochemistry against p21 (brown) with nuclear hemalum coloration (blue). Brown nucleus were considered positives. Lower left panel: Quantification of the percentage of vascular p21-positive cells. Lower right panel: p21-positive cells in lung tissue excluding vessels and bronchus.
Scale bar is 20µm. Data are individual values +mean and SEM. Statistics: *p<0,05 **p<0,005 ***p<0,001 ****p<0,0001 using ANOVA followed by Bonferroni correction for multiple tests.

Figure 3. Analysis of γH2.AX, TIFs and short telomeres in lungs of aged mice.
(**A**) Percentage of the γH2AX-positive cells (left panel) and quantification of the TIFs per nucleus, defined as colocalization of red (γH2AX) and green (Cy3-$(CCCTAA)_3$ PNA probe) signal, (right panel) in the lung parenchyma of the 4 and 18-month-old mice. $p21^{+/+}$ and $p21^{+/Tert}$ are littermates. Each dot represents the mean of 30 nucleus for one mouse. Data are presented as individual values +mean and SEM.
(**B**) Representative IF-FISH images are shown in the right panel. Paraffin lung sections were subjected to the IF-FISH using anti-γH2AX antibody (red) and the Cy3-$(CCCTAA)_3$ PNA probe (green). The nuclei were counterstained with DAPI (blue).
(**C**) Number of short telomeres per genome in lungs from the $p21^{+/+}$ and $p21^{+/Tert}$ littermates (4 and 18-month-old mice). Genomic DNA was extracted from whole lungs and the length of short telomeres was analysed by TeSLA. The fraction of short telomeres for each mouse (n=6 for each group) was estimated from cumulative frequency distributions for the following thresholds: 2.4 kb (red squares), 1.2 kb (yellow squares), 0.6 kb (green triangles) and 0.4 kb (blue circles). No threshold allowed the detection of significant difference using ANOVA. The individual southern blots are shown in Fig. S3.
(D) Correlation between short telomeres per genome (<1.2kb) and the SA-b-Gal positive cells (in %) for each mouse. Data are individual values with linear regression curve.

Figure 4. p21-promoter dependent TERT expression bypasses senescence in PA-SMCs ex-vivo
(A) Cumulative population doubling level (PDL) of pulmonary-artery smooth muscle cells (PA-SMCs) isolated from mice from the three mentioned genotypes. The data points are the means of 8 independent cultures established from individual mice. *p<0,05 comparing $p21^{+/Tert}$ with $p21^{+/+}$ and $p21^{+/-}$, student t-test.
(B) PA-SMC from $p21^{+/+}$ (left) and $p21^{+/Tert}$ (right) littermate mice were observed under the microscope at passage 4. Representative fields were obtained using transmitted light and mCherry filter. Higher magnification of a mCherry-positive cell is shown in the bottom left. Scale bar is 100 µm.

(**C**) Quantification of the *Tert* mRNA levels in PA-SMCs from the $p21^{+/+}$ and $p21^{+/Tert}$ 4-month-old mice (littermates) at early (p4-6) and late (p9-11) passage. Left panel represent the level of endogenous Tert mRNA, right panel represents the level of KI allele. Nearly all *Tert* mRNA is transcribed from the KI allele. The means of three independent measurements are plotted, and the error bars are SEs.
(**D**) Telomerase activity measured by qTRAP at early passages. The data points correspond to vascular PA-SMC cultures established from individual $p21^{+/+}$ and $p21^{+/Tert}$ 4-month-old mice. * $p < 0.05$ from the two-sided *t* test.
(**E**) Analysis of the short telomere fraction by Telomere Shortest Length Assay (TeSLA) in the cultured PA-SMCs from $p21^{+/+}$ and $p21^{+/Tert}$ mice. Left panels depict Southern blots probed for the TTAGGG repeats, and the right panels show quantification of the cumulative number of short telomeres across the telomere length thresholds.

Figure 5. Tert expression under the control of the p21 promoter protects against age-related lung emphysema and fibrosis
(**A**) Emphysema assessment is obtained by measuring the mean linear intercept (MLI) in lungs from 4 and 18-month-old $p21^{+/+}$, $p21^{+/Tert}$ (littermates), and $p21^{+/-}$ mice. Scale bar is 200µm.
(B) Bronchiolar thickness assessment is obtained by measuring the epithelial wall thickness in lungs from young and old mice from the three genotypes. Scale bar is 100µm.
(C) Lung fibrosis assessment is obtained by histopathological analysis using modified Ashcroft scoring on young and old mice from the three genotypes. Scale bar is 200µm.
(A, B, C): Data are individual values +mean and SEM. Statistics: *p<0,05 **p<0,005 ***p<0,001 ****p<0,0001 using ANOVA followed by Bonferroni correction for multiple tests.

Figure 6. Suppression of emphysema in $p21^{+/Tert}$ lungs is associated with vascular cell preservation
18-month-old mice were injected with Bromodeoxyuridin (BrdU) intra-peritoneally 24h before organ sampling.
(**A**) BrdU immunostaining was performed using anti-BrdU antibody in lungs from $p21^{+/+}$ and $p21^{+/Tert}$ littermates mice along with $p21^{+/-}$ mice (upper panel). Positive cells are stained in brown (red arrows). Nucleus were stained using hematoxillin (blue). Middle panel emphases on vessels where most of the BrdU-positive cells were found. L= Vessel lumen. Lower panels show haematoxylin-eosin-safran (HES) staining of the lungs for emphysema assessment.
(**B**) Quantification of BrdU-positive cells in lungs expressed in percentage for the overall lung tissue (left panel) and emphysema assessment by measurement of the mean linear intercept (MLI, in µm).
(**C**) Correlation of the percent of BrdU positive cells and emphysema for each mouse.
(**D**) Measurement of the percentage of SA-β-Gal positive cells (in blue). Left panel: Representative staining of positive cells (red arrow). Right panel: percentage of SA-ß-Gal positive cells for each mouse.
(**E**) Capillary density in lung was assessed in $p21^{+/+}$, $p21^{+/-}$ and $p21^{+/Tert}$ mice aged of 4 and 18-months. Immunofluorescence experiment was performed by using anti-isolectinB4 antibody (red) and DAPI staining (blue). Higher magnification examples of capillaries are presented on the lower right corner of each field. Scale bar is 200µm. Right panel: number of capillaries normalized by the number of DAPI-positive cells.

Data are individual values +mean and SEM. Statistics: *p<0,05 **p<0,005 ***p<0,001 ****p<0,0001 using ANOVA followed by Bonferroni correction for multiple tests.

Figure 7. Emphysema, cellular senescence, and capillary density in old mice expressing a catalytically inactivated TERT ($p21^{+/Tert-CI}$ mice)

18-month-old p21+/Tert and p21+/Tert-CI mice were injected with Bromodeoxyuridin (BrdU) intra-peritoneally 24h before organ sampling and sacrificed. Upper panels are representative micrographs, lower panels are quantifications.

(**A**) Emphysema was assessed by measuring the mean linear intercept (MLI, in µm) on haematoxylin-eosin-Safran stained lungs.

(**B, D, E**) Immonuhistochemistry was performed using anti-p16 (B), anti-p21 (D), and anti-BrdU (E) antibodies (red arrows) with nuclear hemalum counter-staining (blue). Results are expressed as percentage of vascular cells (left) or percentage of alveolar cells (right).

(**C**) SA-β-Gal staining (blue) with nuclear neutral red counter-staining (red). Results are presented as overall percent positive cells.

(**F**) Capillary density was assessed using anti-isolectinB4 antibody (red) with DAPI (blue). Yellow arrows indicate positive signal. Results are presented as the number of capillaries normalized by the number of DAPI-positive cells.

Data are individual values +mean and SEM. Statistics: *p<0,05 **p<0,005 using Mann-Whitney test. Scale bar is 200µm.

Figure 8. A subclass of $p21^{+/Tert}$ endothelial capillary cells shows a transcriptomic signature associated with EC regeneration

(**A**) UMAP clustering of lung endothelial cells from WT, $p21^{+/-}$ and $p21^{+/Tert}$ mice. Cell populations were identified based known markers for these endothelial cell subtypes (Kalucka et al., 2020) (Fig. S8). (Art) artery EC cells; (Cap_1; also called aCap) capillary 1 EC cells; (Cap_2; also called gCap) capillary 2 EC cells (Gillich et al. 2020); (Lym) lymphatic EC cells and (Vein) vein EC cells.

(**B**) Distribution of EC subtypes in $p21^{+/+}$, $p21^{+/-}$ and $p21^{+/Tert}$ mice in percentage.

(**C**) 3D plots of the significant p-values (−log10 p > 1.42) for the DEGs between p21-positive (Cdkn1a > 0) and p21-negative (Cdkn1a = 0) EC from lungs from $p21^{+/+}$, $p21^{+/-}$, and $p21^{+/Tert}$. Genotypes are indicated on the X, Y, and Z axis. The highly significant genes (−log10 p > 4) are shown as red and green dots.

(**D**) Predicted interactions genes identified in (C). The interaction network was downloaded from the STRING database.

(**E**) Triangular heatmap representing the pairwise correlation coefficients (pearson correlation) for the DEG in gCap. Genotypes are indicated in the figure. Genes are ordered according to a hierarchical clustering. Correlation coefficient values are represented according to the indicted colour scale. Coloured rectangles on the right indicate the p.value for each gene after comparison of their expression in p21 positive (Cdkn1a > 0) versus negative (Cdkn1a = 0) gCap cells.

(**F**) UMAP clustering of gCap cells (merge of the 3 genotypes). Note the clear demarcation of two sub clusters, characterized by the number of cells expressing Cdkn1a (p21).

(**G**) % of gCap cells belonging to cluster 1 and 2 for the indicated genotypes

(**H**) Heatmap of DEG in in gCap cells. The dark and light green bars represent cells from cluster 2 and 1, respectively.

Figure 9. T p21$^{+/Tert}$ AT2 cells are enriched in a subclass of AT2 cells expressing markers of epithelial cells sustaining alveolar regeneration

(A) UMAP showing subclusters of AT2 cells. Right panel represents AT2 cell distribution within each cluster.

(B) Heatmap of differentially up-regulated expressed genes (upDEGs) in p21$^{+/Tert}$ AT2 single cells compared to WT and p21$^{+/-}$. Columns represent individual cells grouped by cluster. Light red, green, and blue bars delineate cells from cluster 1, 2 and 3, respectively. Genes are grouped regarding to their expression levels in each cluster (hierarchical clustering on the Pearson correlation between genes). The colour code represents the z-score of expression.

(**C**) Violin plots show gene expression (log2 scale) of only significant upDEGs in single-cell p21$^{+/Tert}$ (red) compare to WT (black) or p21$^{+/-}$ (grey) within each cluster. Dots represent individual cells. Wilcoxon rank-sum test with continuity correction was performed to test significance (*P < 0.05; **P < 0.01; ***P < 0.001).

(**D**) Violin plots show G1-phase score per cell based on the expression of cell cycle-specific markers. AT2 cells are spited according to cluster and genotype (WT (black); p21$^{+/}$ (grey) or p21$^{+/Tert}$ (red)).

Methods

RESOURCE AVAILABILITY

Lead Contact

Further information and requests for resources and reagents should be directed to and will be fulfilled by the Lead Contact, Vincent Geli (vincent.geli@inserm.fr).

Materials Availability

Mouse lines generated in this study are deposited at Ciphe, Marseille, France. Details and code numbers appear in the Supplementary information. This study did not generate unique reagents.

Data and Code Availability

Original data for single cell RNA-sequencing is available at the Gene Expression Omnibus (GEO).

EXPERIMENTAL MODEL AND SUBJECT DETAILS

Ethical statement

Mice were used according to institutional guidelines, which complied with national and international regulations. All animals received care according to institutional guidelines, and all experiments were approved by the Institutional Ethics committee number 16, Paris, France (licence number 16-093).

Mice

Mice were bred and maintained in specific-pathogen-free conditions with sterilized food and water provided ad libitum and were maintained on a 12 h light and 12 h dark cycle in accordance with institutional guidelines. Male mice were used in this study, at the age of 4 (young group) and 18 (old group) month old. After genotyping, $p21^{+/+}$ and $p21^{+/Tert}$ mice from each litter were randomly assigned to the young or old group until the sufficient number of individuals per group was reached. $P21^{+/-}$ mice generated at the same time in the same conditions followed the same procedure.

Primary pulmonary artery smooth muscle cells

Pulmonary artery smooth muscle were extracted and cultured as already described (Houssaini et al., 2018). Cells were cultured at 37°C, 5% O2, in DMEM (High glucose, -Pyruvate, Gibco) supplemented with 10%(v/v) decomplemented FBS and 1%(v/v) Penicillin-Streptomycin.

METHOD DETAILS

mCherry-2A-mTert vector and mice generation

A 6,4 kb genomic fragment encompassing coding exons 2 and 3 of the *Cdkn1a* gene was isolated from a BAC clone of B6 origin (clone n° RP23-412O16; http://www.lifesciences.sourcebioscience.com) and subcloned into the *Not* I site of pBluescript II. The genomic sequence containing the homologous arms was checked by DNA sequencing. A synthetic gene encoding the mCherry, 2A peptide, and the 5' coding region of mTert (beyond the *Sac* II site) was constructed by gene synthesis (By DNA2.0 Inc) to produce the mCherry-2A-mTert^{SacII} cassette. Using ET recombination, the synthetic mCherry-2A-mTert^{SacII} cassette

was introduced in the 5' coding region of the *Cdkn1a* gene replacing the start codon. The full-length mTert was next introduced in the mCherry-2A-mTert^{SacII} truncated cassette by inserting into the targeting vector a synthetic mTert (*Sac* II-*EcoR* I) fragment restoring the full-length mTert to give rise to the complete mCherry-2A-mTert cassette. A self-deleter NeoR cassette was further introduced in the *EcoR* I site of the targeting vector immediately after the mTert sequence. A cassette coding for the diphtheria toxin fragment A expression cassette was finally introduced in the *Not* I site of the targeting vector. All the elements of the final targeting are shown in Fig. S1A.

JM8.F6 C57BL/6N ES cells were electroporated with the targeting vector linearized with Fse1 (Pettitt et al., 2009). The scheme of the introduction of the mCherry-2A-mTert-Neo^{R} cassette in place of the ATG codon of Cdkn1a is shown in Fig. S1B. After selection with G418, ES cell clones were screened for proper homologous recombination. The correct integration of the cassette was verified by Southern blot with a Cdkn1a probe (Fig. S1C) and by long range PCR (Fig. S1D). The primers used to check the correct insertion of the cassette were:

1310_ScES_01 Fwd: 5' CTGAATGAACTGCAGGACGA ;

1310_ScES_01_Rev : 5' CTTGCCTATATTGCTCAAGG.

To ensure that adventitious non-homologous recombination events had not occurred in the selected ES clones, a Southern blot was performed with a mCherry probe (Fig. S1E).

Properly recombined ES cells were injected into Balb/c blastocysts. Germline transmission led to the self-excision of the loxP-Cre-NeoR-loxP cassette in male germinal cells. p21-mCherry-2A-mTert mice (p21$^{+/Tert}$) were identified by PCR of tail DNA. The primers used for genotyping were as follows: sense-WT 5'-GCTGAACTCAACACCCACCT-3', sense-p21-Tert 5'-GGACCTCTGAGGACAGCCCAAA-3' and antisense 5'-GCAGCAGGGCAGAGGAAGTA-3'. The resulting PCR products were 435 (WT) and 520 (p21$^{+/Tert}$) base pairs long. The proteins produced by the mRNA mcherry-2A-mTert polycistronic mRNA are shown in Fig S1F. In the final construct, Cdkn1a protein is no further produced from the mutated allele because of the substitution of the C*dkn1a* [ATG] codon by the cassette and the presence of a STOP codon at the end of Tert.

As control mice, we developed p21$^{+/+}$ littermates and p21$^{+/-}$ mice that were obtained by crossing the p21 homozygous knockout strain B6.129S6(Cg)-*Cdkn1a*^{tm1led}/J (from JAX laboratories) with isogenic p21$^{+/+}$ mice. In the p21$^{+/-}$ mouse, a neo cassette replaces exon 2 of *Cdkn1a*. Homozygotes are viable, fertile, and of normal size.

p21$^{+/TertCI}$ mice were constructed with exactly the same targeting vector used to construct p21$^{+/Tert}$ except that the codon GAT in *Tert* coding for D702 has been changed into GCA coding for A. Primers to genotype p21$^{+/Tert}$ and p21$^{+/TertCI}$ mice are indicated in Supplemental Information.

Verification of the TERT activity

To check that TERT expressed from the mCherry-2A-mTert can produce active telomerase, the mCherry-2A-mTert was amplified by PCR (S 5'-atatatgaattcatggtgagcaagggcgaggaggata; AS 5'- atatatgcggccgcttagtccaaaatggtctgaaagtct) from the targeting vector and cloned into the *EcoR* I/*Not* I sites of pCAG-GFP. In the resulting vector, the mCherry-2A-mTert cassette is expressed under the control of the

strong constitutive CAG promoter. The resulting vector was transfected in the mTert-/- mouse ES cells (provided by Lea Harrington, Montreal). Prior to transfection, the Neo^R cassette in the Tert-/- ES cells was disrupted by CRISPR/CAS9 since the Tert-/- ES cells and the electroporated plasmid shared the same antibiotic resistance. The presence of telomerase activity was analysed in the cell extracts using the Telomere Repeat Amplification Protocol (TRAP) (see below). We could detect robust telomerase activity in mouse ES mTert-/- transfected by the construct pCAG-mCherry-2A-mTert (Fig. S2A).

Fluorescence imaging of mice and organs

To next demonstrate *in vivo* the expression of the KI *Cdkn1a* allele in response to p21 promoter activation, littermate $p21^{+/+}$ and $p21^{+/Tert}$ mice were exposed either to a whole body ionizing radiation or to doxorubicin which both activate the p53-p21 axis of the DNA damage response (DDR) (Yang et al., 2014).

For irradiation experiments, $p21^{+/+}$ and $p21^{+/Tert}$ mice were imaged (time zero) and then exposed to 1.5-Gy of total body irradiation (RX, RS2000 Irradiator, Radsources). Non-invasive whole-body fluorescence (FLI) was determined at the indicated times post-treatment. Imaging was performed using a Photon-IMAGER (Biospace Lab), and mice were anesthetized with 3 % vetflurane through an O_2 flow modulator for 5 min and then the image was acquired (4-s exposure, excitation=545nm, background=495nm, emission filter cut off=615nm). Corresponding color-scale photographs and color fluorescent images were superimposed and analyzed with M3vision (Biospace Lab) image analysis software.

For Doxorubicin treatments, the $p21^{+/+}$ and $p21^{+/Tert}$ mice were injected i.p. with doxorubicin (DXR) (20 mg/kg). Doxorubicin has been shown to activate p21 promoter to high levels in the liver and kidneys (Ohtani et al., 2007). 24h after DXR injection, mice were then sacrificed and organs were rapidly removed and imaged within 15 min of sacrifice (4-s exposure). After that, proteins and RNA were extracted from kidneys and liver for immunoblot (p21) and RT-qPCR (Tert) analyses, respectively.

PA-SMC culture

Pulmonary artery smooth muscle were extracted and cultured as already described (Houssaini et al., 2018). At each passage, cells were counted and 50,000 cells were put back in culture in a 25 cm2 flask and cultured in DMEM supplemented with FBS. Representative images of cells in culture were obtained using EVOS M5000 Imaging System (ThermoFisher) on $p21^{+/+}$ and $p21^{+/Tert}$ cells 24h after plating on a 24 well plate.

Animal preparation and lung histological analysis

Two groups of mice from the three genotypes were prepared in order to sacrifice 4-month-old mice and 18-month-old mice at the same time. To reach the final mice number per group and per genotype, this experiment was reproduced three individual times, on three independent cohort. For $p21^{+/Tert\text{-}CI}$ mice, an independent cohort of $p21^{+/Tert}$ and $p21^{+/Tert\text{-}CI}$ mice was prepared. After mice sacrifice three lobes of the right lung were quickly removed and immediately snap-frozen in liquid nitrogen then stored at -80°C for biological measurements. Genomic DNA from the right lung of each animal was used for TESLA assay. The last lobe of the right lung was fixed with 2% formaldehyde (Sigma) and 0.2% glutaraldehyde (Sigma) for 45 minutes.

Then, lungs were washed with PBS and stained in a titrated pH 6 solution containing 40 mM citric acid, 150 mM NaCl, 2 mM $MgCl_2$, 5 mM potassium ferrocyanide, and 1 mg/ml X-Gal. Stained lobes were then imbedded in paraffin and 5μm thick sections were cut. After counter coloration of the nucleus with neutral red, 10 fields per section were acquired at an overall magnification of 500.
The left lungs were fixed by intratracheal infusion of 4% paraformaldehyde aqueous solution (Sigma) at a trans-pleural pressure of 30 cmH_2O. For morphometry studies, 5 µm–thick sagittal sections along the greatest axis of the left lung were cut in a systematic manner to allow immunostaining. Lung emphysema was measured using mean linear intercept methods on hematoxylin-eosin-safran (HES) coloration as described by Weibel and Cruz-Drive. Briefly 20 fields/animal light microscope fields at an overall magnification of 500, were overlapped with a 42-point, 21-line eyepiece according to a systematic sampling method from a random starting point. To correct area values for shrinkage associated with fixation and paraffin processing, we used a factor of 1.22, calculated during a previous study. On the same fields, bronchial thickness was measured using ImageJ software on bronchus with lumen diameter <130μm. Ashcroft score was assessed as already described (Hübner et al., 2008) on HES sections.

Immunohistochemistry and immunofluorescence

For immunohistochemistry, slides were deparaffinized using HistoChoice (Sigma) and rehydrated using increasing concentration of ethanol. After antigen retrieval (10min, 95°C in citrate buffer, pH6) and cellular permeabilization (0.1% Triton X-100 in PBS, 10min), slides were incubated for 60 minutes in 1% BSA and 5% goat serum in PBS and then incubated overnight with anti-p21 antibody (BD Pharmingen, mouse, #556431) and anti-p16 antibody (abbiotec, rabbit, #250804). We used the ABC Vectastain kit (Vector Labs, Burlingame, CA) to mark the primary antibodies according to the user's guide. The staining substrate was diaminobenzidine (FastDAB, Sigma-Aldrich, St. Louis, MO), and the sections were counterstained with hemalun. After counterstaining sections were mounted with coverslips.
For immunofluorescence, slides were incubated with citrate buffer 10mM at pH6 for 20min at 95C. Slides were then incubated with 2.5% horse serum (Vector Laboratory, S-2000) for 30min at 37°C, and then incubated with anti-isolectin B4 alexafluor 594 antibody (I21413, ThermoFischer Scientific), 2μg/ml in 2.5% horse serum. Slides were mounted with DAPI and observed under the microscope at a 20x magnification. For all immunostaining, 10 fields per lung were used for quantification.

BrdU intraperitoneal injection and analysis

A subgroup of mice received an intraperitoneal injection of 5-bromo-2'-deoxyuridine (ab142567, abcam) diluted in PBS at 25mg/ml. Mice received 100mg/kg BrdU 24h prior to sacrifice by cervical dislocation. Organ samples were collected and fixed in formalin solution, then embedded in paraffin. BrdU immunostaining was performed following provider instruction, using BrdU immunohistochemistry kit (ab125306, abcam).

Telomere dysfunction Induced Foci (TIFs)

Paraffin–embedded lung tissue sections (5 µm wide) were dewaxed in xylene (2x5min), re-hydrated in a graded ethanol series (5min each) and PBS (5min). Epitope demasking was

performed in 10mM NaCitrate, 0.05% Tween-20, pH=6.0, at 95°C for 30min, upon which the slides were rinced in water, and tissue sections de-hydrated in 96% ethanol, and air dried. Telomeric PNA-probe (Alexa488-OO-$(TTAGGG)_3$, from PANAGENE) was diluted in hybridisation buffer (70% formamide, 10mM Tris, pH=7.2, 1% Blocking Reagent (ROCHE, 11095176001; stock solution : 10% (w/v) Blocking Reagent in 0.1M Maleic acid, 0.15M NaCl, pH=7.5) at a final concentration of 0.5µM. The probe was then denatured 5 min at 95°C, and put on ice (2min). 100µL of denatured probe was then put on the tissue sections, under sealed coverslip, and probe and target were denatured a further 4min at 80°C, on a hot plate. Hybridization was in a moist chamber, overnight, in the dark, at room temperature (RT). All further incubations and washes were also performed in the dark.
Post-hybridisation washes were in 70% formamide, 10mM Tris, pH=7.2, 30min, and 50mM Tris, 150mM NaCl, 0.05% Tween-20, pH7.5, 15min at RT. Slides were rinced in PBS, and blocked in 4% BSA in PBS, 0.1% Tween-20 for 1h at RT. Primary antibody incubation (Mouse mab anti phospho-Histone H2A.X (Ser139), clone JBW301 ; 05-636, MILLIPORE) was 1/200 in 4% BSA in PBS, 0.1% Tween-20, overnight at 4°C. Washes were in PBST (PBS, 0.1% Tween-20), 30min, RT. Secondary antibody incubation (Donkey polyclonal anti Mouse Alexa555, A31570, THERMO FISHER SCIENTIFIC) was 1/500 in 4% BSA in PBS, 0.1% Tween-20, 2h at 37°C. Washes were in PBST, 30min, RT. Slides were finally rinced in PBS and mounted in VectaShield containing DAPI (H-1200, VECTOR LABORATORIES).
Images were recorded with a DeltaVision Elite Deconvolution microscope (GE Healthcare Bio-Sciences Corp.). The microscope is equipped with a CCD sCMOS monochromatic camera (2048x2048 pixels, 6,45µm x 6,45µm, 15 Bit), and 3D-image stacks were taken (1024x1024 pixels, 115 optical sections around the focal plane, at 0.35µm interval) with an OLYMPUS objective (60x, NA 1.42, oil). Images were deconvolved and analysed with softWoRx Software. Total DNA damage (total number of phospho-Histone H2A.X (Ser139) spots), and TIFs (colocalisation between γH2A.X and telomeric spots) were assessed manually on orthogonal projections (Maximum Brightness Projection) of the deconvolved image stacks.

RNA extraction, RT-qPCR, and Western blots

Total RNA was extracted using the method of (Chomczynski and Sacchi, 1987) with reagents included in the RNeasy kit (Qiagen). To exclude contamination with genomic DNA, the RNA was treated with DNase I directly on mini columns. Reverse transcription was performed using 0.5 to 2.0 µg of RNA, 50 ng/µL random hexamers, and 200 U of Superscript IV (Invitrogen) in the 20 µL reaction volume for 15 min at 55°C, followed by inactivation for 10 min at 80°C. The resulting cDNA was diluted 5-20 fold and analyzed by real-time qPCR using the SYBR Green master mix (Takara bio) and 400 nanomolar each of the following primers: mTert-2253S 5'-AGCCAAGGCCAAGTCCACAA and mTert-2399A 5'-AGAGATGCTCTGCTCGATGACA to target all *Tert* transcripts/isoforms; 2A-F2 5'-AGCAGGAGATGTTGAAGAAAACCC and mTert-5'R25'-GGCCACACCTCCCGGTATC to target *mCherry-2A-Tert* transcript from the KI *Cdkn1a* allele; mActb-90S 5'-ACACCCGCCACCAGTTCG and mActb-283A 5'-GGCCTCGTCACCCACATAGG to target β actin transcript. At least one primer within each pair was designed to anneal onto the exon-

exon junction to avoid priming on genomic DNA, and the specificity of amplification was verified on agarose gel.
Immunoblots were carried out using standard procedures. The membranes were incubated with primary antibodies followed by incubation with the secondary HRP conjugates, and the signal was detected using an enhanced chemiluminescence detection system (GE Healthcare). The unsaturated images were acquired using ChemiDoc MP imaging system (Bio-Rad), and the signal densities were quantified using Image Studio Lite ver 5.2 (LI-COR). Antibodies used were rabbit monoclonal anti-p21 [EPR3993] (abcam) and mouse anti-b-actin (SigmaAldrich A1978) antibody.

Telomere Repeat Amplification Protocol (TRAP)

To measure telomerase activity in cellular/tissue extracts TRAP was performed according to the original protocol (Kim and Wu, 1997; Kim et al., 1994). Briefly, the cells or tissues were extracted on ice using standard CHAPS buffer (60 µL per 10^6 cells) supplemented with a cocktail of protease inhibitors (Roche) and 20 units of RNase inhibitor (Applied Biosystems) followed by centrifugation at 18000 x g for 30 min at 4°C. The protein concentration in the supernatant was quantified using Pierce™ 660nm Protein Assay and the aliquots equivalent to 800, 400, and 200 ng of protein were used to extend 50 ng of the telomerase substrate (TS oligo) in the 25 µL reaction volume. For gel-based detection of the TRAP product we used FAM-labeled TS and the standard ACX and NT primers (Kim and Wu, 1997) to amplify the telomerase extension products and the internal TSNT control, respectively. For the real-time qPCR-based TRAP we used unlabeled TS and the ACX primer alone. The qTRAP was performed using the SYBR Green PCR mix, and the amount of CHAPS extracts was optimized by serial dilutions.

Telomere Shortest Length Assay (TeSLA)

TeSLA was performed according to the protocol described by (Lai et al., 2017). Briefly, 50 ng of undigested genomic DNA was ligated with an equimolar mixture (50 pM each) of the six TeSLA-T oligonucleotides containing seven nucleotides of telomeric C-rich repeats at the 3′ end and 22 nucleotides of the unique sequence at the 5’ end. After overnight ligation at 35°C, genomic DNA was digested with *Cvi*AII, *Bfa*I, *Nde*I, and *Mse*I, the restriction enzymes creating either AT or TA overhangs. Digested DNA was then treated with Shrimp Alkaline Phosphatase to remove 5′ phosphate from each DNA fragment to avoid their ligation to each other during the subsequent adapter ligation. Upon heat-inactivation of phosphatase, partially double-stranded AT and TA adapters were added (final concentration 1 µM each) and ligated to the dephosphorylated fragments of genomic DNA at 16°C overnight. Following ligation of the adapters, genomic DNA was diluted to 20 pg/µL, and 2-4 µL was used in a 25 µL PCR reaction to amplify terminal fragments using primers complementary to the unique sequences at the 5’ ends of the TeSLA-T oligonucleotides and the AT/TA adapters. FailSafe polymerase mix (Epicenter) with 1× FailSafe buffer H was used to amplify G-rich telomeric sequences. Entire PCR reactions were then loaded onto the 0.85% agarose gel for separation of the amplified fragments. To visualize telomeric fragments, the DNA was transferred from the gel onto the nylon membrane by Southern blotting procedure and hybridized with the ^{32}P-labeled

$(CCCTAA)_3$ probe. The sizes of the telomeric fragments were quantified using TeSLA Quant software (Lai et al., 2017).

Single cell RNAseq

Isolation of lung single cells from 18 month-old p21$^{+/+}$, p21$^{+/-}$ and p21$^{+/Tert}$ mice . Mouse trachea is injected with 1,5ml dispase 50 U/ml (Corning #354235) followed by 0,5 ml agarose 1%. Lung is resected and minced in 3 ml DPBS 1x $CaCl^{2+}$ and $MgCl^{2+}$ (Gibco, 14040-091). Collagenase/dispase 100 mg/ml (Roche #11097113001) is added to the chopped tissue and placed on a rotator at 37 °C for 30 min. Enzymatic activity is inhibited by adding 5 ml of DPBS 1x (Gibco, 14190-094) containing 10% FBS and 1mM EDTA (Sigma #E7889). Cell suspension is filtered through 100 µm nylon cell strainer (Fisher Scientific #11893402), treated by DNase I (Sigma D4527) and filtered again through a 40 µm nylon cell strainer (Fisher Scientific #11873402). Red blood cells are removed by red blood cell lysis (Invitrogen, 00-4333-57) treatment for 90s at room temperature. Finally, lung cells are centrifuged at 150*g*, 4 °C for 6 min, resuspended in DPBS 1x containing 0,02% BSA (Pan Biotech #P06-13911000) and counted in a Malassez.

Preparation of single cell sequencing libraries. Single-cell 3'-RNA-Seq samples were prepared using single cell V2 reagent kit and loaded in the Chromium controller according to standard manufacturer protocol (10x Genomics, PN-120237) to capture 6.000 cells. Briefly, dissociated lung cells are encapsulated using microfluidic device. RNAs are captured on beads coated of oligos containing an oligo-dTTT, UMIs and a specific barcode. After reverse transcription, cDNAs are washed, PCR-amplified and washed again before analysis on a Bioanalyzer (Agilent) for quality control. Finally, libraries are prepared following standard Illumina protocol and sequenced on a NovaSeq sequencer (Illumina). Raw sequences are demultiplexed and reads are mapped onto the mm10 reference genome using the v2.3 Cell Ranger pipeline (10X Genomics) to generate a count matrix for each sample.

Quality control and Normalization of the single-cell data. The digital matrices were filtered from ambient contaminating RNA using the SoupX package (version 1.4.8) (preprint biorxiv:(Young and Behjati, 2020)). Further filtering was done to remove low-quality cells with low UMI counts, doublets and cells with relatively high mitochondrial DNA content. Outlier analysis was performed with perCellQCMetrics from the scatter package. An upper cutoff was manually determined for each sample based on a plot of gene count versus UMI count or % of mitochondrial genes, to have at least 1000 UMIs, number of transcripts ranging between 1000 and 30000 and at most 14% mitochondrial transcripts. The quality was consistent across samples, and differences in RNA and gene content could be ascribed to cell-type-specific effects. DGE matrices from all samples (p21$^{+/+}$, p21$^{+/-}$ and p21$^{+/Tert}$) sequenced simultaneously were merged and subsequently normalized using the deconvolution normalization method in the *scran R* package in order to correct for differences in read depth and library size inside and between samples.

Clustering, cell type, and cycle annotation. Seurat v3.2.2 was used to perform dimensionality reduction, clustering, and visualization on the unique combined (with all samples) and normalized matrix. After scaling the data, dimensionality reduction was performed using PCA on the highly variable genes. Seurat's *FindNeighbors* function was run to identify cluster markers with the following parameters: reduction = "pca" and dims = 1:10, followed by the

FindClusters function with resolution = 1. The Seurat function *RunUMAP* was used to generate 2-dimensional umap projections using the top principal components detected in the dataset. To annotate cells, we mapped each cluster to the Mouse Cell Atlas (Han et al., 2018) by using the *scMCA* function (Sun et al., 2019). Cluster identities were further verified according to gene markers found with the *FindMarkers* function from Seurat. Doublet cells were identified manually as expressing markers for different cell types and the doublet subgroups were removed from the matrix. In order to define endothelial (EC) and AT2 cells subclusters, EC and AT2 cell classes were isolated and subjected to a new clustering by the *FindNeighbors* function with new parameters: reduction = "pca" and dims (1:15 for EC and 1:10 for AT2 cells). Seurat *FindAllMarkers* function was applied to each EC subclusters and the markers were compared to the top 50 gene markers previously found in lung EC (Kalucka et al., 2020). We thus annotated EC subclusters depending on the enrichment of marker genes and identified five subtypes of EC (artery, capillary_1, capillary_2, vein and lymphatic). We annotated two functionally divergent lung EC capillary clusters according to (Gillich et al., 2020). We thus reassign EC capillary_1 as "aCap" and EC capillary_2 as "gCap". In order to assign cell cycle phase to each cell, we used the Cyclone method to our single cell RNA-Seq dataset.

Differential gene expression analysis. To identify differentially expressed genes, we used the Mann-Whitney test adjusted by the Benjamini & Hochberg (BH) method. When comparing 18 month-old $p21^{+/+}$, $p21^{+/-}$ and $p21^{+/Tert}$ EC expressing Cdkn1a (normalized count >0) versus those not expressing Cdkn1a (normalized count =0), significant genes were defined according to their adjusted p-value (< 0.05) and by the fact that these genes were expressed in at least 10% of the cells. For 3D representation (Fig. 8C), genes expressed in EC with –LOG(p.value)>4 only in the $p21^{+/Tert}$ but not in the $p21^{+/+}$, $p21^{+/-}$ were considered for subsequent analysis.

String analysis (https://string-db.org) was performed to investigate interactions between the significant genes.

Pearson correlation analysis. Pearson correlation analysis was carried using a matrix of normalized counts per cell for each selected gene expressed in gCap cells. We performed pairwise-comparisons between the selected genes in 225, 323 or 265 cells from $p21^{+/+}$, $p21^{+/-}$ and $p21^{+/Tert}$ gCap cells, respectively.

QUANTIFICATION AND STATISTICAL ANALYSIS

Basic statistics, tests for the differences between the means, and one-way analysis of variance (ANOVA) were performed with the GraphPad Prism 7 Software. ANOVA followed by Bonferroni multiple comparison test was used to compare the means of more than two independent groups. Pairwise correlation and multiple regression analyses were performed using Statistica 13.0 software package (StatSoft/Dell).

References

Alder, J.K., Guo, N., Kembou, F., Parry, E.M., Anderson, C.J., Gorgy, A.I., Walsh, M.F., Sussan, T., Biswal, S., Mitzner, W., et al. (2011). Telomere length is a determinant of emphysema susceptibility. Am. J. Respir. Crit. Care Med. *184*, 904–912.

Alder, J.K., Barkauskas, C.E., Limjunyawong, N., Stanley, S.E., Kembou, F., Tuder, R.M., Hogan, B.L.M., Mitzner, W., and Armanios, M. (2015). Telomere dysfunction causes alveolar stem cell failure. Proc. Natl. Acad. Sci. *112*, 5099–5104.

Amsellem, V., Gary-Bobo, G., Marcos, E., Maitre, B., Chaar, V., Validire, P., Stern, J.-B., Noureddine, H., Sapin, E., Rideau, D., et al. (2011). Telomere dysfunction causes sustained inflammation in chronic obstructive pulmonary disease. Am. J. Respir. Crit. Care Med. *184*, 1358–1366.

Angelidis, I., Simon, L.M., Fernandez, I.E., Strunz, M., Mayr, C.H., Greiffo, F.R., Tsitsiridis, G., Ansari, M., Graf, E., Strom, T.-M., et al. (2019). An atlas of the aging lung mapped by single cell transcriptomics and deep tissue proteomics. Nat. Commun. *10*, 963.

Armanios, M., and Blackburn, E.H. (2012). The telomere syndromes. Nat. Rev. Genet. *13*, 693–704.

Armanios, M.Y., Chen, J.J.-L., Cogan, J.D., Alder, J.K., Ingersoll, R.G., Markin, C., Lawson, W.E., Xie, M., Vulto, I., Phillips, J.A., et al. (2007). Telomerase mutations in families with idiopathic pulmonary fibrosis. N. Engl. J. Med. *356*, 1317–1326.

Barnes, P.J. (2016). Inflammatory mechanisms in patients with chronic obstructive pulmonary disease. J. Allergy Clin. Immunol. *138*, 16–27.

Bernardes de Jesus, B., Vera, E., Schneeberger, K., Tejera, A.M., Ayuso, E., Bosch, F., and Blasco, M.A. (2012). Telomerase gene therapy in adult and old mice delays aging and increases longevity without increasing cancer. EMBO Mol. Med. *4*, 691–704.

Birch, J., Anderson, R.K., Correia-Melo, C., Jurk, D., Hewitt, G., Marques, F.M., Green, N.J., Moisey, E., Birrell, M.A., Belvisi, M.G., et al. (2015). DNA damage response at telomeres contributes to lung aging and chronic obstructive pulmonary disease. Am. J. Physiol. Lung Cell. Mol. Physiol. *309*, L1124-1137.

Boyer, L., Savale, L., Boczkowski, J., and Adnot, S. (2014). [Cellular senescence and pulmonary disease: COPD as an example]. Rev. Mal. Respir. *31*, 893–902.

Breau, M., Houssaini, A., Lipskaia, L., Abid, S., Born, E., Marcos, E., Czibik, G., Attwe, A., Beaulieu, D., Palazzo, A., et al. The antioxidant N-acetylcysteine protects from lung emphysema but induces lung adenocarcinoma in mice. JCI Insight *4*.

Campisi, J. (2013). Aging, cellular senescence, and cancer. Annu. Rev. Physiol. *75*, 685–705.

Carow, B., and Rottenberg, M.E. (2014). SOCS3, a Major Regulator of Infection and Inflammation. Front. Immunol. *5*, 58.

Cheng, T., Rodrigues, N., Shen, H., Yang, Y., Dombkowski, D., Sykes, M., and Scadden, D.T. (2000). Hematopoietic stem cell quiescence maintained by p21cip1/waf1. Science *287*, 1804–1808.

Childs, B.G., Durik, M., Baker, D.J., and van Deursen, J.M. (2015). Cellular senescence in aging and age-related disease: from mechanisms to therapy. Nat. Med. *21*, 1424–1435.

Chomczynski, P., and Sacchi, N. (1987). Single-step method of RNA isolation by acid guanidinium thiocyanate-phenol-chloroform extraction. Anal. Biochem. *162*, 156–159.

Cordasco, E., Beerel, F., Vance, J., Wende, R., and Toffolo, R.R. (1968). Newer Aspects of the Pulmonary Vasculature in Chronic Lung Disease. Angiology.

Dagouassat, M., Gagliolo, J.-M., Chrusciel, S., Bourin, M.-C., Duprez, C., Caramelle, P., Boyer, L., Hue, S., Stern, J.-B., Validire, P., et al. (2013). The cyclooxygenase-2-prostaglandin E2 pathway maintains senescence of chronic obstructive pulmonary disease fibroblasts. Am. J. Respir. Crit. Care Med. *187*, 703–714.

Dunnill, M.S. (1962). Quantitative Methods in the Study of Pulmonary Pathology. Thorax *17*, 320–328.

El-Deiry, W.S. (2016). p21(WAF1) Mediates Cell-Cycle Inhibition, Relevant to Cancer Suppression and Therapy. Cancer Res. *76*, 5189–5191.
Engeland, K. (2018). Cell cycle arrest through indirect transcriptional repression by p53: I have a DREAM. Cell Death Differ. *25*, 114–132.
d'Adda di Fagagna, F., Reaper, P.M., Clay-Farrace, L., Fiegler, H., Carr, P., Von Zglinicki, T., Saretzki, G., Carter, N.P., and Jackson, S.P. (2003). A DNA damage checkpoint response in telomere-initiated senescence. Nature *426*, 194–198.
Fouillade, C., Curras-Alonso, S., Giuranno, L., Quelennec, E., Heinrich, S., Bonnet-Boissinot, S., Beddok, A., Leboucher, S., Karakurt, H.U., Bohec, M., et al. (2020). FLASH Irradiation Spares Lung Progenitor Cells and Limits the Incidence of Radio-induced Senescence. Clin. Cancer Res. *26*, 1497–1506.
Fouquerel, E., Barnes, R.P., Uttam, S., Watkins, S.C., Bruchez, M.P., and Opresko, P.L. (2019). Targeted and Persistent 8-Oxoguanine Base Damage at Telomeres Promotes Telomere Loss and Crisis. Mol. Cell *75*, 117-130.e6.
Gartel, A.L., and Tyner, A.L. (1999). Transcriptional regulation of the p21((WAF1/CIP1)) gene. Exp. Cell Res. *246*, 280–289.
Gillich, A., Zhang, F., Farmer, C.G., Travaglini, K.J., Tan, S.Y., Gu, M., Zhou, B., Feinstein, J.A., Krasnow, M.A., and Metzger, R.J. (2020). Capillary cell-type specialization in the alveolus. Nature *586*, 785–789.
Han, X., Wang, R., Zhou, Y., Fei, L., Sun, H., Lai, S., Saadatpour, A., Zhou, Z., Chen, H., Ye, F., et al. (2018). Mapping the Mouse Cell Atlas by Microwell-Seq. Cell *172*, 1091-1107.e17.
Harper, J.W., Elledge, S.J., Keyomarsi, K., Dynlacht, B., Tsai, L.H., Zhang, P., Dobrowolski, S., Bai, C., Connell-Crowley, L., and Swindell, E. (1995). Inhibition of cyclin-dependent kinases by p21. Mol. Biol. Cell *6*, 387–400.
Herbig, U., Jobling, W.A., Chen, B.P.C., Chen, D.J., and Sedivy, J.M. (2004). Telomere shortening triggers senescence of human cells through a pathway involving ATM, p53, and p21(CIP1), but not p16(INK4a). Mol. Cell *14*, 501–513.
Hergenreider, E., Heydt, S., Tréguer, K., Boettger, T., Horrevoets, A.J.G., Zeiher, A.M., Scheffer, M.P., Frangakis, A.S., Yin, X., Mayr, M., et al. (2012). Atheroprotective communication between endothelial cells and smooth muscle cells through miRNAs. Nat. Cell Biol. *14*, 249–256.
Hoffmeyer, K., Raggioli, A., Rudloff, S., Anton, R., Hierholzer, A., Del Valle, I., Hein, K., Vogt, R., and Kemler, R. (2012). Wnt/β-catenin signaling regulates telomerase in stem cells and cancer cells. Science *336*, 1549–1554.
Hoppstädter, J., and Ammit, A.J. (2019). Role of Dual-Specificity Phosphatase 1 in Glucocorticoid-Driven Anti-inflammatory Responses. Front. Immunol. *10*, 1446.
Houben, J.M.J., Mercken, E.M., Ketelslegers, H.B., Bast, A., Wouters, E.F., Hageman, G.J., and Schols, A.M.W.J. (2009). Telomere shortening in chronic obstructive pulmonary disease. Respir. Med. *103*, 230–236.
Houssaini, A., Breau, M., Kebe, K., Abid, S., Marcos, E., Lipskaia, L., Rideau, D., Parpaleix, A., Huang, J., Amsellem, V., et al. (2018). mTOR pathway activation drives lung cell senescence and emphysema. JCI Insight *3*.
Huang, K., Rabold, R., Schofield, B., Mitzner, W., and Tankersley, C.G. (2007). Age-dependent changes of airway and lung parenchyma in C57BL/6J mice. J. Appl. Physiol. Bethesda Md 1985 *102*, 200–206.
Hübner, R.-H., Gitter, W., El Mokhtari, N.E., Mathiak, M., Both, M., Bolte, H., Freitag-Wolf, S., and Bewig, B. (2008). Standardized quantification of pulmonary fibrosis in histological samples. BioTechniques *44*, 507–511, 514–517.
Kalucka, J., de Rooij, L.P.M.H., Goveia, J., Rohlenova, K., Dumas, S.J., Meta, E., Conchinha, N.V., Taverna, F., Teuwen, L.-A., Veys, K., et al. (2020). Single-Cell Transcriptome Atlas of Murine Endothelial Cells. Cell *180*, 764-779.e20.

Karimian, A., Ahmadi, Y., and Yousefi, B. (2016). Multiple functions of p21 in cell cycle, apoptosis and transcriptional regulation after DNA damage. DNA Repair *42*, 63–71.
Kasahara, Y., Tuder, R.M., Taraseviciene-Stewart, L., Le Cras, T.D., Abman, S., Hirth, P.K., Waltenberger, J., and Voelkel, N.F. (2000). Inhibition of VEGF receptors causes lung cell apoptosis and emphysema. J. Clin. Invest. *106*, 1311–1319.
Kasahara, Y., Tuder, R.M., Cool, C.D., Lynch, D.A., Flores, S.C., and Voelkel, N.F. (2001). Endothelial cell death and decreased expression of vascular endothelial growth factor and vascular endothelial growth factor receptor 2 in emphysema. Am. J. Respir. Crit. Care Med. *163*, 737–744.
Kathiriya, J.J., Brumwell, A.N., Jackson, J.R., Tang, X., and Chapman, H.A. (2020). Distinct Airway Epithelial Stem Cells Hide among Club Cells but Mobilize to Promote Alveolar Regeneration. Cell Stem Cell *26*, 346-358.e4.
Khachigian, L.M., Lindner, V., Williams, A.J., and Collins, T. (1996). Egr-1-induced endothelial gene expression: a common theme in vascular injury. Science *271*, 1427–1431.
Kim, N.W., and Wu, F. (1997). Advances in quantification and characterization of telomerase activity by the telomeric repeat amplification protocol (TRAP). Nucleic Acids Res. *25*, 2595–2597.
Kim, C.F.B., Jackson, E.L., Woolfenden, A.E., Lawrence, S., Babar, I., Vogel, S., Crowley, D., Bronson, R.T., and Jacks, T. (2005). Identification of bronchioalveolar stem cells in normal lung and lung cancer. Cell *121*, 823–835.
Kim, N.W., Piatyszek, M.A., Prowse, K.R., Harley, C.B., West, M.D., Ho, P.L., Coviello, G.M., Wright, W.E., Weinrich, S.L., and Shay, J.W. (1994). Specific association of human telomerase activity with immortal cells and cancer. Science *266*, 2011–2015.
Kim, S.-J., Shan, P., Hwangbo, C., Zhang, Y., Min, J.-N., Zhang, X., Ardito, T., Li, A., Peng, T., Sauler, M., et al. (2019). Endothelial toll-like receptor 4 maintains lung integrity via epigenetic suppression of p16INK4a. Aging Cell *18*, e12914.
Kippin, T.E., Martens, D.J., and van der Kooy, D. (2005). p21 loss compromises the relative quiescence of forebrain stem cell proliferation leading to exhaustion of their proliferation capacity. Genes Dev. *19*, 756–767.
Kobayashi, K., Ichihara, Y., Tano, N., Fields, L., Murugesu, N., Ito, T., Ikebe, C., Lewis, F., Yashiro, K., Shintani, Y., et al. (2018). Fibrin Glue-aided, Instant Epicardial Placement Enhances the Efficacy of Mesenchymal Stromal Cell-Based Therapy for Heart Failure. Sci. Rep. *8*, 9448.
Lai, T.-P., Zhang, N., Noh, J., Mender, I., Tedone, E., Huang, E., Wright, W.E., Danuser, G., and Shay, J.W. (2017). A method for measuring the distribution of the shortest telomeres in cells and tissues. Nat. Commun. *8*, 1356.
Liu, Q., Liu, K., Cui, G., Huang, X., Yao, S., Guo, W., Qin, Z., Li, Y., Yang, R., Pu, W., et al. (2019). Lung regeneration by multipotent stem cells residing at the bronchioalveolar-duct junction. Nat. Genet. *51*, 728–738.
López-Otín, C., Blasco, M.A., Partridge, L., Serrano, M., and Kroemer, G. (2013). The Hallmarks of Aging. Cell *153*, 1194–1217.
Martínez, P., and Blasco, M.A. (2017). Telomere-driven diseases and telomere-targeting therapies. J. Cell Biol. *216*, 875–887.
Matmati, S., Lambert, S., Géli, V., and Coulon, S. (2020). Telomerase Repairs Collapsed Replication Forks at Telomeres. Cell Rep. *30*, 3312-3322.e3.
McDonald, A.I., Shirali, A.S., Aragón, R., Ma, F., Hernandez, G., Vaughn, D.A., Mack, J.J., Lim, T.Y., Sunshine, H., Zhao, P., et al. (2018). Endothelial Regeneration of Large Vessels is a Biphasic Process Driven by Local Cells with Distinct Proliferative Capacities. Cell Stem Cell *23*, 210-225.e6.
Mercado, N., Ito, K., and Barnes, P.J. (2015). Accelerated ageing of the lung in COPD: new concepts. Thorax *70*, 482–489.
Michaudel, C., Fauconnier, L., Julé, Y., and Ryffel, B. (2018). Functional and morphological differences of the lung upon acute and chronic ozone exposure in mice. Sci. Rep. *8*, 10611.
Ohtani, N., Imamura, Y., Yamakoshi, K., Hirota, F., Nakayama, R., Kubo, Y., Ishimaru, N.,

Takahashi, A., Hirao, A., Shimizu, T., et al. (2007). Visualizing the dynamics of p21(Waf1/Cip1) cyclin-dependent kinase inhibitor expression in living animals. Proc. Natl. Acad. Sci. U. S. A. *104*, 15034–15039.
Parimon, T., Yao, C., Stripp, B.R., Noble, P.W., and Chen, P. (2020). Alveolar Epithelial Type II Cells as Drivers of Lung Fibrosis in Idiopathic Pulmonary Fibrosis. Int. J. Mol. Sci. *21*.
Parrinello, S., Samper, E., Krtolica, A., Goldstein, J., Melov, S., and Campisi, J. (2003). Oxygen sensitivity severely limits the replicative lifespan of murine fibroblasts. Nat. Cell Biol. *5*, 741–747.
Pettitt, S.J., Liang, Q., Rairdan, X.Y., Moran, J.L., Prosser, H.M., Beier, D.R., Lloyd, K.C., Bradley, A., and Skarnes, W.C. (2009). Agouti C57BL/6N embryonic stem cells for mouse genetic resources. Nat. Methods *6*, 493–495.
Povedano, J.M., Martinez, P., Flores, J.M., Mulero, F., and Blasco, M.A. (2015). Mice with Pulmonary Fibrosis Driven by Telomere Dysfunction. Cell Rep. *12*, 286–299.
Povedano, J.M., Martinez, P., Serrano, R., Tejera, Á., Gómez-López, G., Bobadilla, M., Flores, J.M., Bosch, F., and Blasco, M.A. (2018a). Therapeutic effects of telomerase in mice with pulmonary fibrosis induced by damage to the lungs and short telomeres. ELife *7*.
Povedano, J.M., Martinez, P., Serrano, R., Tejera, Á., Gómez-López, G., Bobadilla, M., Flores, J.M., Bosch, F., and Blasco, M.A. (2018b). Therapeutic effects of telomerase in mice with pulmonary fibrosis induced by damage to the lungs and short telomeres. ELife *7*.
Ranchoux, B., Harvey, L.D., Ayon, R.J., Babicheva, A., Bonnet, S., Chan, S.Y., Yuan, J.X.-J., and Perez, V. de J. (2018). Endothelial dysfunction in pulmonary arterial hypertension: an evolving landscape (2017 Grover Conference Series). Pulm. Circ. *8*, 2045893217752912.
Reddy, S.P.M., and Mossman, B.T. (2002). Role and regulation of activator protein-1 in toxicant-induced responses of the lung. Am. J. Physiol. Lung Cell. Mol. Physiol. *283*, L1161-1178.
Salwig, I., Spitznagel, B., Vazquez-Armendariz, A.I., Khalooghi, K., Guenther, S., Herold, S., Szibor, M., and Braun, T. (2019). Bronchioalveolar stem cells are a main source for regeneration of distal lung epithelia in vivo. EMBO J. *38*.
Savale, L., Chaouat, A., Bastuji-Garin, S., Marcos, E., Boyer, L., Maitre, B., Sarni, M., Housset, B., Weitzenblum, E., Matrat, M., et al. (2009). Shortened telomeres in circulating leukocytes of patients with chronic obstructive pulmonary disease. Am. J. Respir. Crit. Care Med. *179*, 566–571.
Schichl, Y.M., Resch, U., Hofer-Warbinek, R., and de Martin, R. (2009). Tristetraprolin impairs NF-kappaB/p65 nuclear translocation. J. Biol. Chem. *284*, 29571–29581.
Ségal-Bendirdjian, E., and Geli, V. (2019). Non-canonical Roles of Telomerase: Unraveling the Imbroglio. Front. Cell Dev. Biol. *7*, 332.
Sharma, G., and Goodwin, J. (2006). Effect of aging on respiratory system physiology and immunology. Clin. Interv. Aging *1*, 253–260.
Shu, J., Li, D., Ouyang, H., Huang, J., Long, Z., Liang, Z., Chen, Y., Chen, Y., Zheng, Q., Kuang, M., et al. (2017). Comparison and evaluation of two different methods to establish the cigarette smoke exposure mouse model of COPD. Sci. Rep. *7*, 15454.
Smogorzewska, A., and de Lange, T. (2002). Different telomere damage signaling pathways in human and mouse cells. EMBO J. *21*, 4338–4348.
Spella, M., Lilis, I., Pepe, M.A., Chen, Y., Armaka, M., Lamort, A.-S., Zazara, D.E., Roumelioti, F., Vreka, M., Kanellakis, N.I., et al. (2019). Club cells form lung adenocarcinomas and maintain the alveoli of adult mice. ELife *8*, e45571.
Stanley, A.J., Hasan, I., Crockett, A.J., van Schayck, O.C.P., and Zwar, N.A. (2014). COPD Diagnostic Questionnaire (CDQ) for selecting at-risk patients for spirometry: a cross-sectional study in Australian general practice. NPJ Prim. Care Respir. Med. *24*, 14024.
Sun, H., Zhou, Y., Fei, L., Chen, H., and Guo, G. (2019). scMCA: A Tool to Define Mouse Cell Types Based on Single-Cell Digital Expression. Methods Mol. Biol. Clifton NJ *1935*, 91–96.
Taniguchi, K., and Karin, M. (2018). NF-κB, inflammation, immunity and cancer: coming of age. Nat. Rev. Immunol. *18*, 309–324.

Tinkum, K.L., Marpegan, L., White, L.S., Sun, J., Herzog, E.D., Piwnica-Worms, D., and Piwnica-Worms, H. (2011). Bioluminescence Imaging Captures the Expression and Dynamics of Endogenous p21 Promoter Activity in Living Mice and Intact Cells . Mol. Cell. Biol. *31*, 3759–3772.
Totzke, G., Essmann, F., Pohlmann, S., Lindenblatt, C., Jänicke, R.U., and Schulze-Osthoff, K. (2006). A novel member of the IkappaB family, human IkappaB-zeta, inhibits transactivation of p65 and its DNA binding. J. Biol. Chem. *281*, 12645–12654.
Tsuji, T., Aoshiba, K., and Nagai, A. (2010). Alveolar cell senescence exacerbates pulmonary inflammation in patients with chronic obstructive pulmonary disease. Respir. Int. Rev. Thorac. Dis. *80*, 59–70.
Voelkel, N.F., Gomez-Arroyo, J., and Mizuno, S. (2011). COPD/Emphysema: The Vascular Story. Pulm. Circ. *1*, 320–326.
Watson, J.K., Sanders, P., Dunmore, R., Rosignoli, G., Julé, Y., Rawlins, E.L., Mustelin, T., May, R., Clarke, D., and Finch, D.K. (2020). Distal lung epithelial progenitor cell function declines with age. Sci. Rep. *10*, 10490.
Yang, F., Teves, S.S., Kemp, C.J., and Henikoff, S. (2014). Doxorubicin, DNA torsion, and chromatin dynamics. Biochim. Biophys. Acta *1845*, 84–89.
Young, M.D., and Behjati, S. (2020). SoupX removes ambient RNA contamination from droplet-based single-cell RNA sequencing data. GigaScience *9*.
Zhang, H., Taylor, W.R., Joseph, G., Caracciolo, V., Gonzales, D.M., Sidell, N., Seli, E., Blackshear, P.J., and Kallen, C.B. (2013). mRNA-binding protein ZFP36 is expressed in atherosclerotic lesions and reduces inflammation in aortic endothelial cells. Arterioscler. Thromb. Vasc. Biol. *33*, 1212–1220.
Zheng, D., Limmon, G.V., Yin, L., Leung, N.H.N., Yu, H., Chow, V.T.K., and Chen, J. (2013). A cellular pathway involved in Clara cell to alveolar type II cell differentiation after severe lung injury. PloS One *8*, e71028.

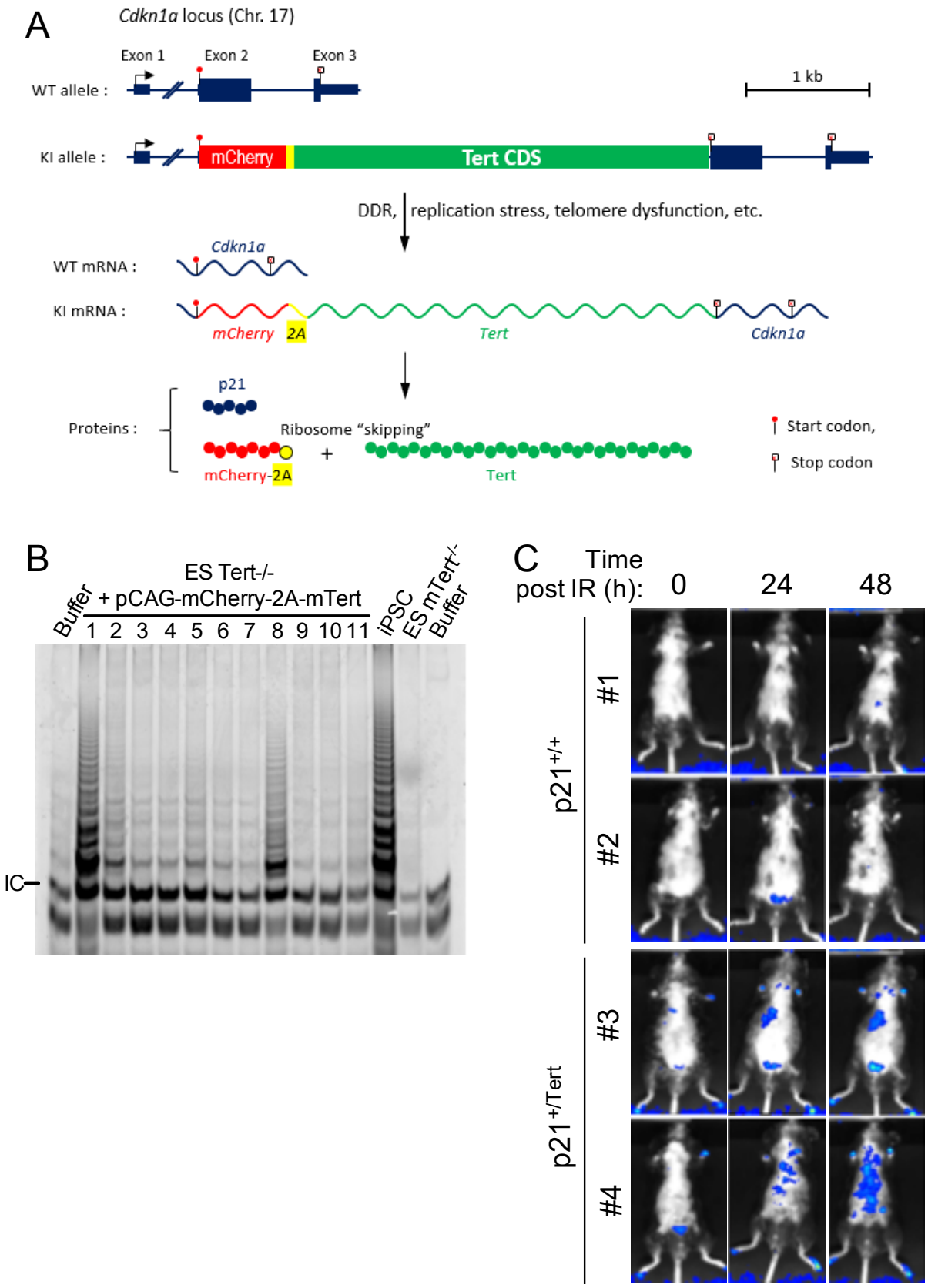
A
Cdkn1a locus (Chr. 17)
Exon 1
Exon 2
Exon 3
WT allele :
1 kb
KI allele :
mCherry
Tert CDS
DDR, replication stress, telomere dysfunction, etc.
WT mRNA :
Cdkn1a
KI mRNA :
mCherry
2A
Tert
Cdkn1a
Proteins :
p21
Ribosome "skipping"
mCherry-2A
+
Tert
Start codon,
Stop codon
B
ES Tert-/-
+ pCAG-mCherry-2A-mTert
Buffer
1 2 3 4 5 6 7 8 9 10 11
iPSC
ES mTert-/-
Buffer
IC
C
Time post IR (h):
0
24
48
p21+/+
#1
#2
p21+/Tert
#3
#4

Figure 1

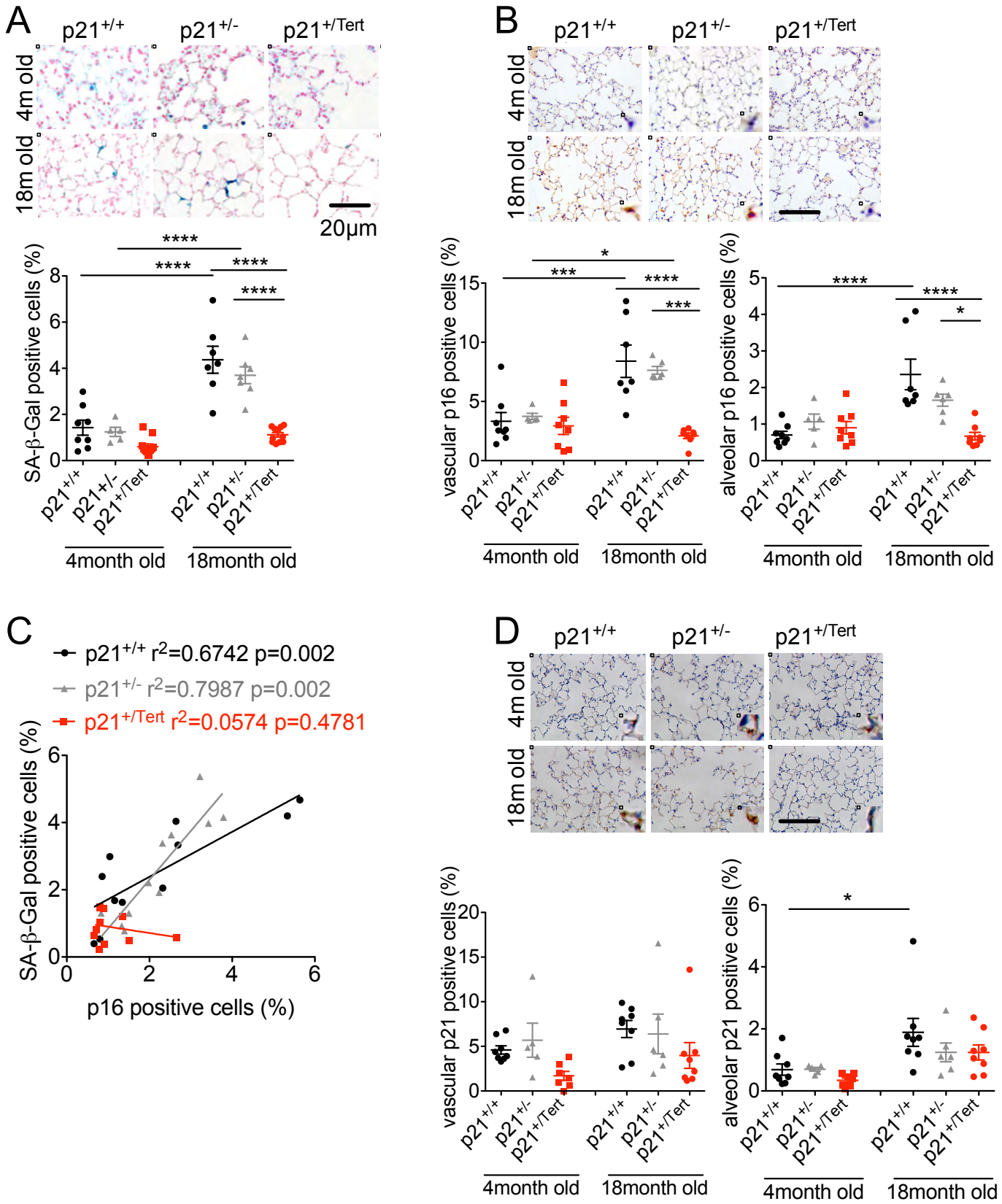
A
p21+/+
p21+/-
p21+/Tert
4m old
18m old
20µm
SA-β-Gal positive cells (%)
4month old
18month old
B
vascular p16 positive cells (%)
alveolar p16 positive cells (%)
C
p21+/+ r2=0.6742 p=0.002
p21+/- r2=0.7987 p=0.002
p21+/Tert r2=0.0574 p=0.4781
SA-β-Gal positive cells (%)
p16 positive cells (%)
D
vascular p21 positive cells (%)
alveolar p21 positive cells (%)

Figure 2

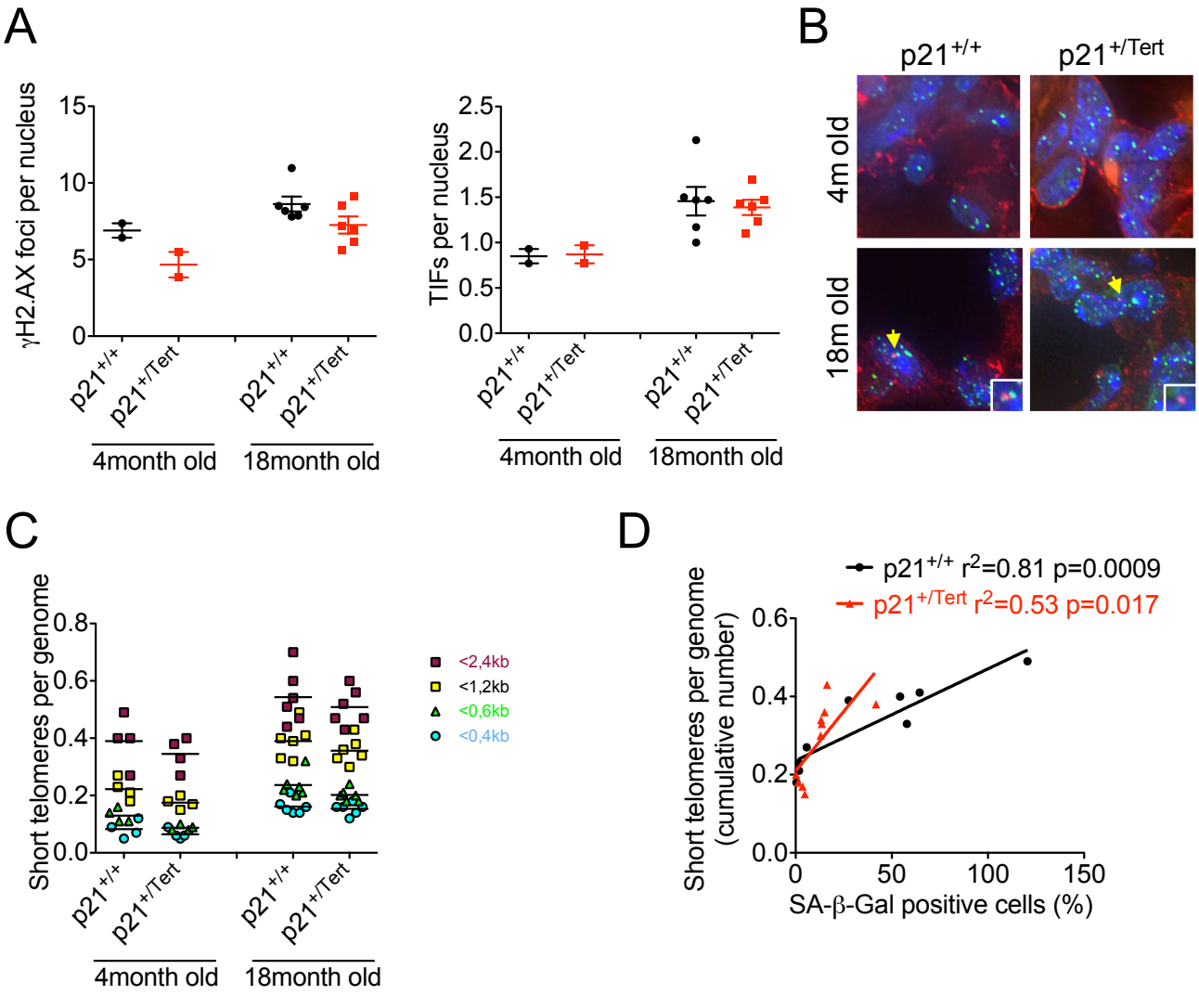
A
γH2.AX foci per nucleus
15
10
5
0
p21+/+
p21+/Tert
p21+/+
p21+/Tert
4month old
18month old
TIFs per nucleus
2.5
2.0
1.5
1.0
0.5
0.0
p21+/+
p21+/Tert
p21+/+
p21+/Tert
4month old
18month old
B
p21+/+
p21+/Tert
4m old
18m old
C
Short telomeres per genome
0.8
0.6
0.4
0.2
0.0
p21+/+
p21+/Tert
p21+/+
p21+/Tert
4month old
18month old
<2,4kb
<1,2kb
<0,6kb
<0,4kb
D
p21+/+ r2=0.81 p=0.0009
p21+/Tert r2=0.53 p=0.017
Short telomeres per genome (cumulative number)
0.6
0.4
0.2
0.0
0
50
100
150
SA-β-Gal positive cells (%)

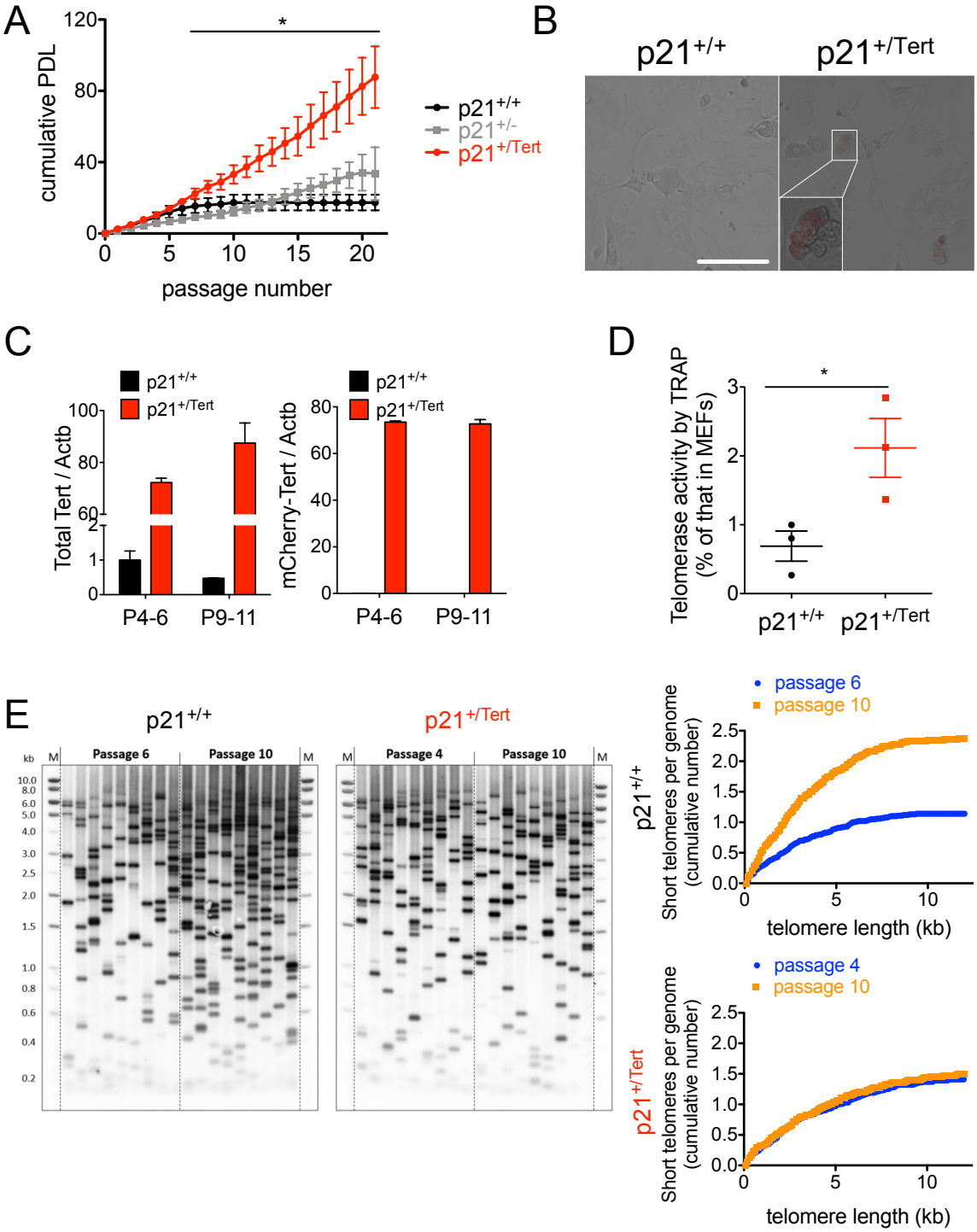
A
cumulative PDL
passage number
p21+/+
p21+/-
p21+/Tert
B
p21+/+
p21+/Tert
C
Total Tert / Actb
mCherry-Tert / Actb
P4-6
P9-11
D
Telomerase activity by TRAP (% of that in MEFs)
E
Passage 6
Passage 10
Passage 4
kb
Short telomeres per genome (cumulative number)
telomere length (kb)
passage 6
passage 10
passage 4

Figure 4

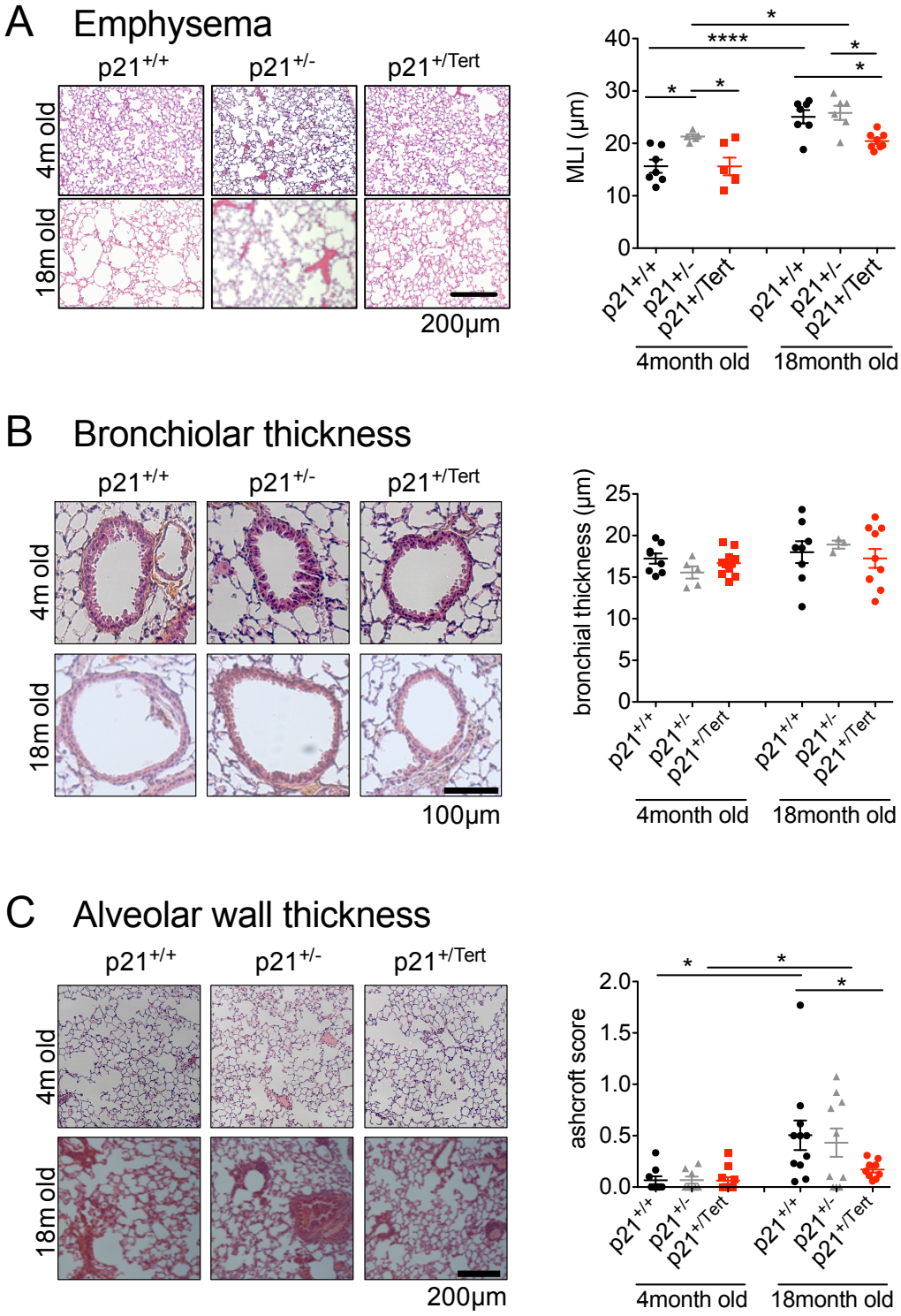
A
Emphysema
p21+/+
p21+/-
p21+/Tert
4m old
18m old
200µm
MLI (µm)
40
30
20
10
0
*
****
*
*
*
*
p21+/+
p21+/-
p21+/Tert
p21+/+
p21+/-
p21+/Tert
4month old
18month old
B
Bronchiolar thickness
p21+/+
p21+/-
p21+/Tert
4m old
18m old
100µm
bronchial thickness (µm)
25
20
15
10
5
0
p21+/+
p21+/-
p21+/Tert
p21+/+
p21+/-
p21+/Tert
4month old
18month old
C
Alveolar wall thickness
p21+/+
p21+/-
p21+/Tert
4m old
18m old
200µm
ashcroft score
2.0
1.5
1.0
0.5
0.0
*
*
*
p21+/+
p21+/-
p21+/Tert
p21+/+
p21+/-
p21+/Tert
4month old
18month old

Figure 5

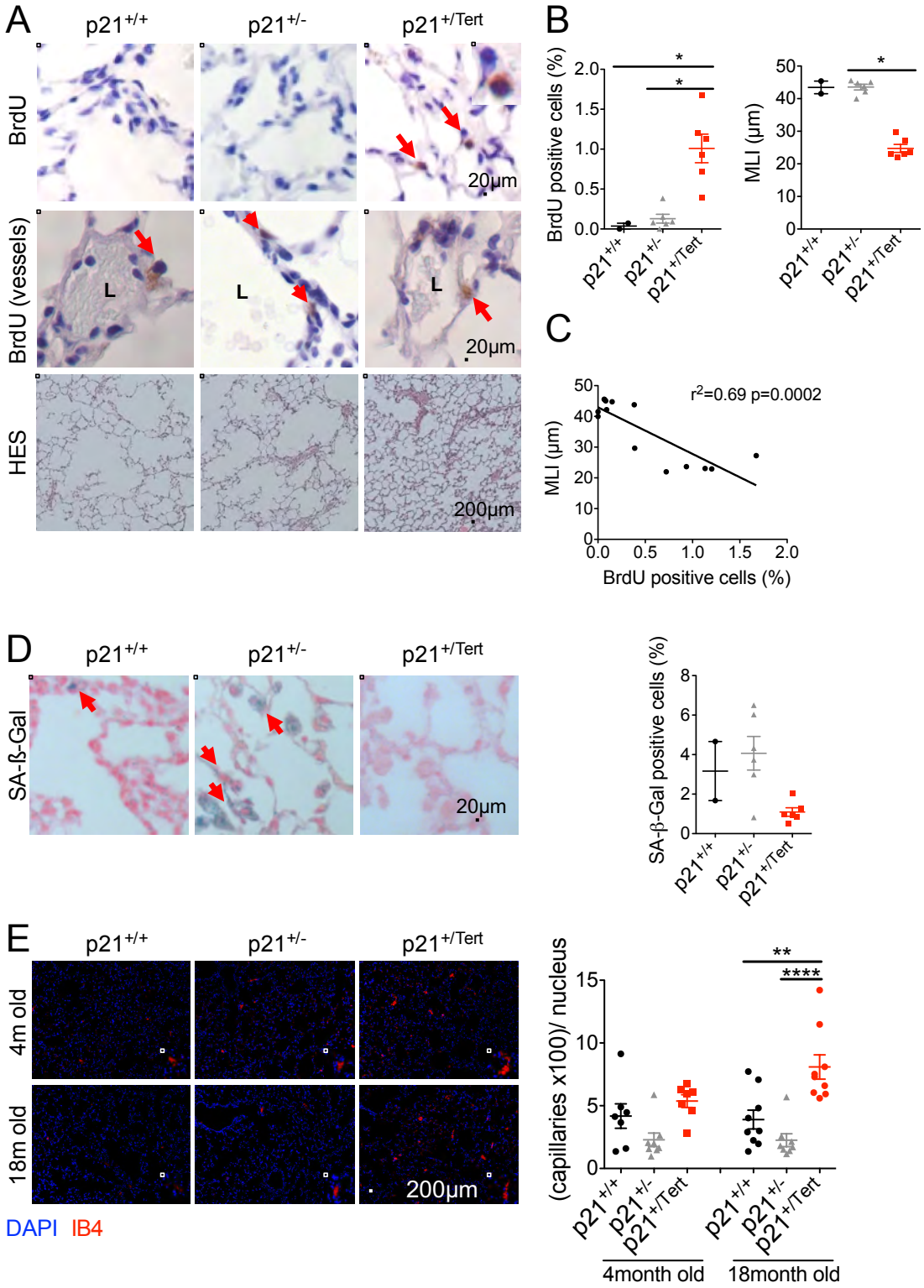
A
p21+/+
p21+/-
p21+/Tert
BrdU
BrdU (vessels)
HES
L
20µm
200µm
B
BrdU positive cells (%)
MLI (µm)
C
r2=0.69 p=0.0002
MLI (µm)
BrdU positive cells (%)
D
SA-ß-Gal
SA-β-Gal positive cells (%)
E
4m old
18m old
DAPI IB4
(capillaries x100)/ nucleus
4month old
18month old

Figure 6

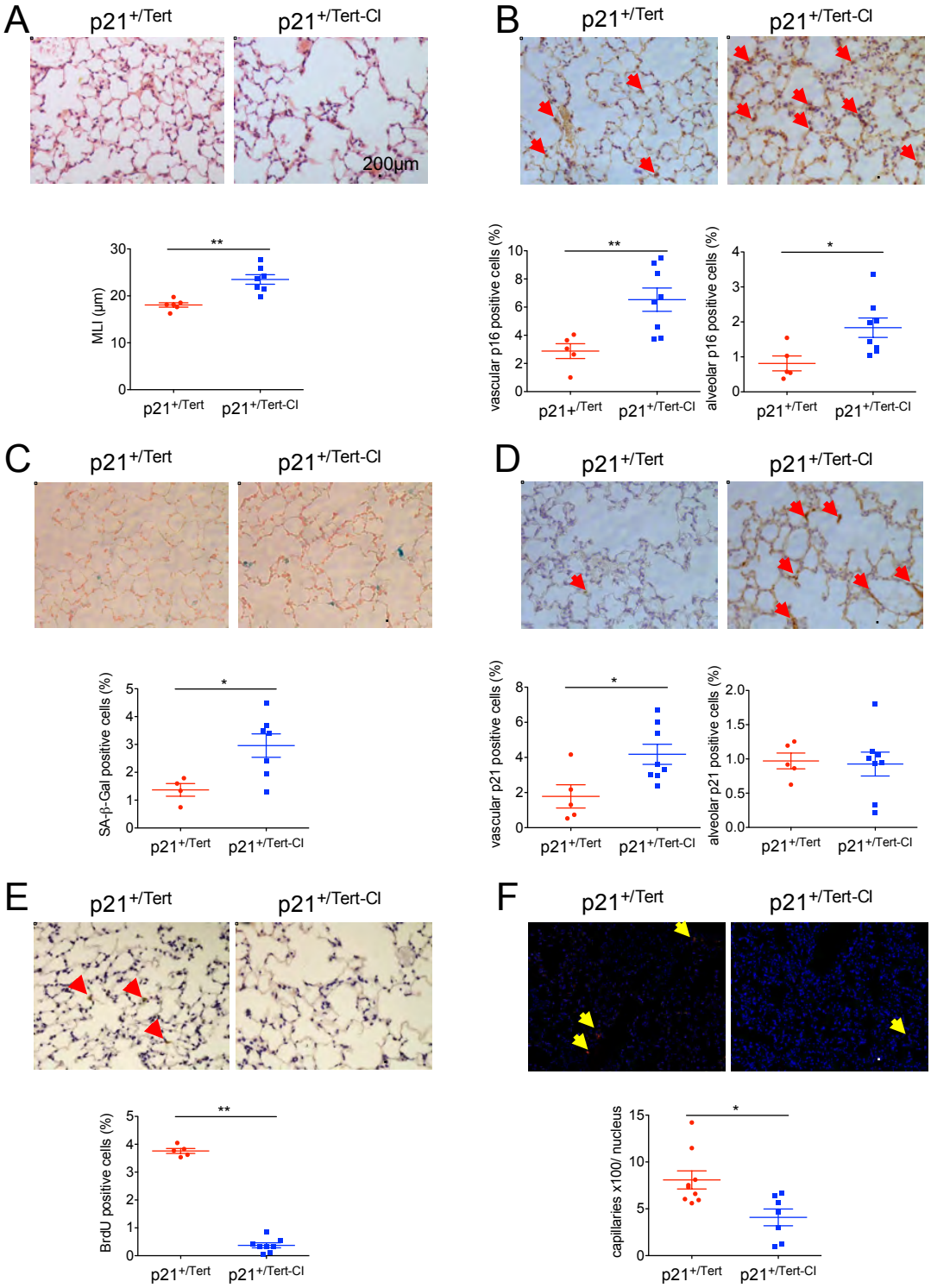
A
p21+/Tert
p21+/Tert-Cl
200μm
MLI (μm)
B
vascular p16 positive cells (%)
alveolar p16 positive cells (%)
C
SA-β-Gal positive cells (%)
D
vascular p21 positive cells (%)
alveolar p21 positive cells (%)
E
BrdU positive cells (%)
F
capillaries x100/ nucleus

Figure 7

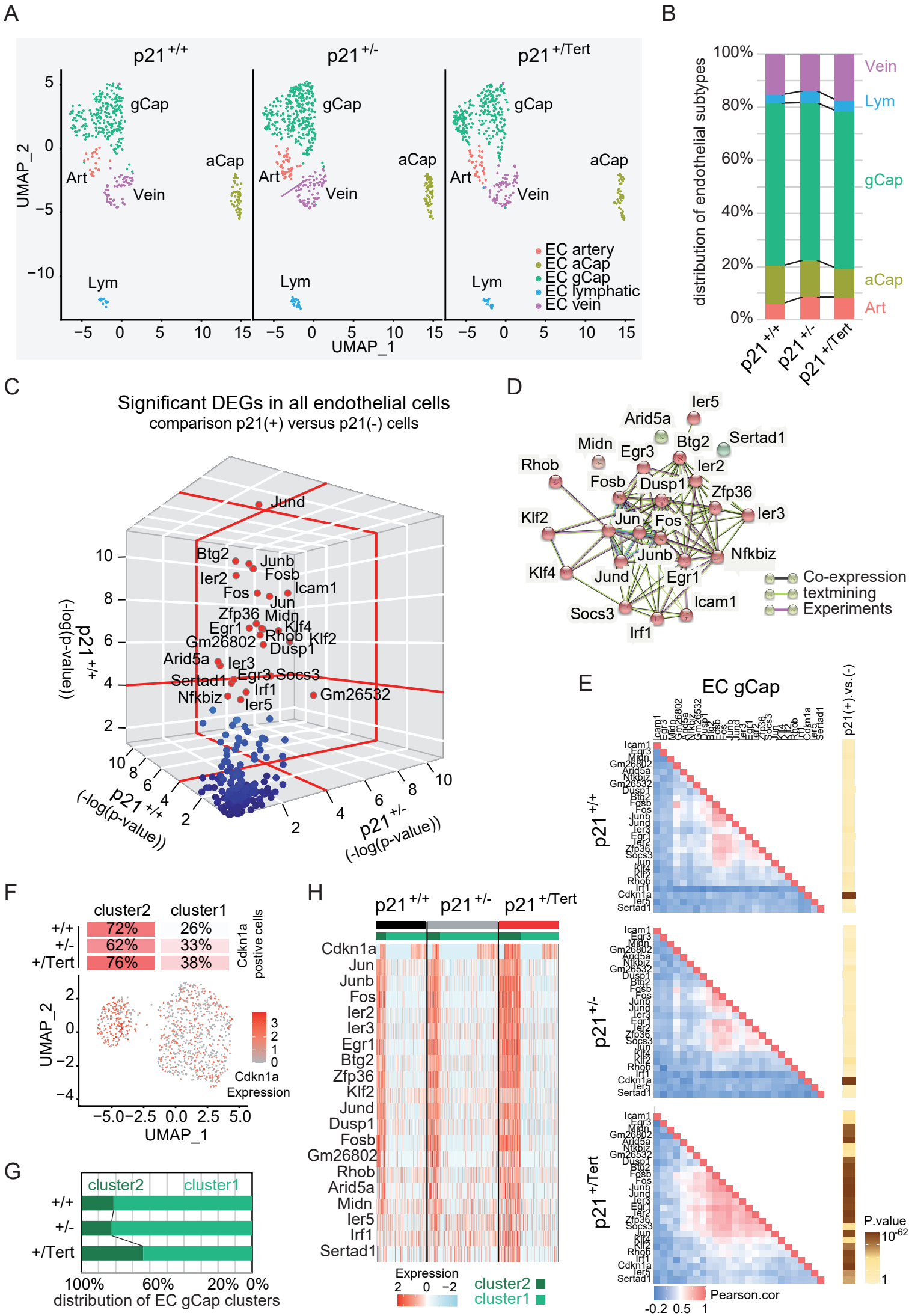
A
p21 +/+
p21 +/-
p21 +/Tert
gCap
aCap
Art
Vein
Lym
UMAP_2
UMAP_1
EC artery
EC aCap
EC gCap
EC lymphatic
EC vein
B
distribution of endothelial subtypes
100%
80%
60%
40%
20%
0%
Vein
Lym
gCap
aCap
Art
C
Significant DEGs in all endothelial cells
comparison p21(+) versus p21(-) cells
p21 +/+ (-log(p-value))
p21 +/- (-log(p-value))
Jund
Btg2
Junb
Fosb
Ier2
Icam1
Fos
Jun
Zfp36
Midn
Egr1
Klf4
Rhob
Klf2
Gm26802
Dusp1
Arid5a
Ier3
Sertad1
Egr3
Socs3
Irf1
Nfkbiz
Ier5
Gm26532
D
Ier5
Arid5a
Sertad1
Midn
Egr3
Btg2
Rhob
Ier2
Fosb
Dusp1
Zfp36
Klf2
Jun
Fos
Ier3
Junb
Nfkbiz
Klf4
Jund
Egr1
Icam1
Socs3
Irf1
Co-expression
textmining
Experiments
E
EC gCap
p21(+).vs.(-)
p21 +/+
p21 +/-
p21 +/Tert
P.value
Pearson.cor
F
cluster2
cluster1
+/+ 72% 26%
+/- 62% 33%
+/Tert 76% 38%
Cdkn1a postive cells
UMAP_2
UMAP_1
Cdkn1a Expression
G
cluster2
cluster1
+/+
+/-
+/Tert
100%
60%
20%
0%
distribution of EC gCap clusters
H
p21 +/+
p21 +/-
p21 +/Tert
Cdkn1a
Jun
Junb
Fos
Ier2
Ier3
Egr1
Btg2
Zfp36
Klf2
Jund
Dusp1
Fosb
Gm26802
Rhob
Arid5a
Midn
Ier5
Irf1
Sertad1
Expression
cluster2
cluster1

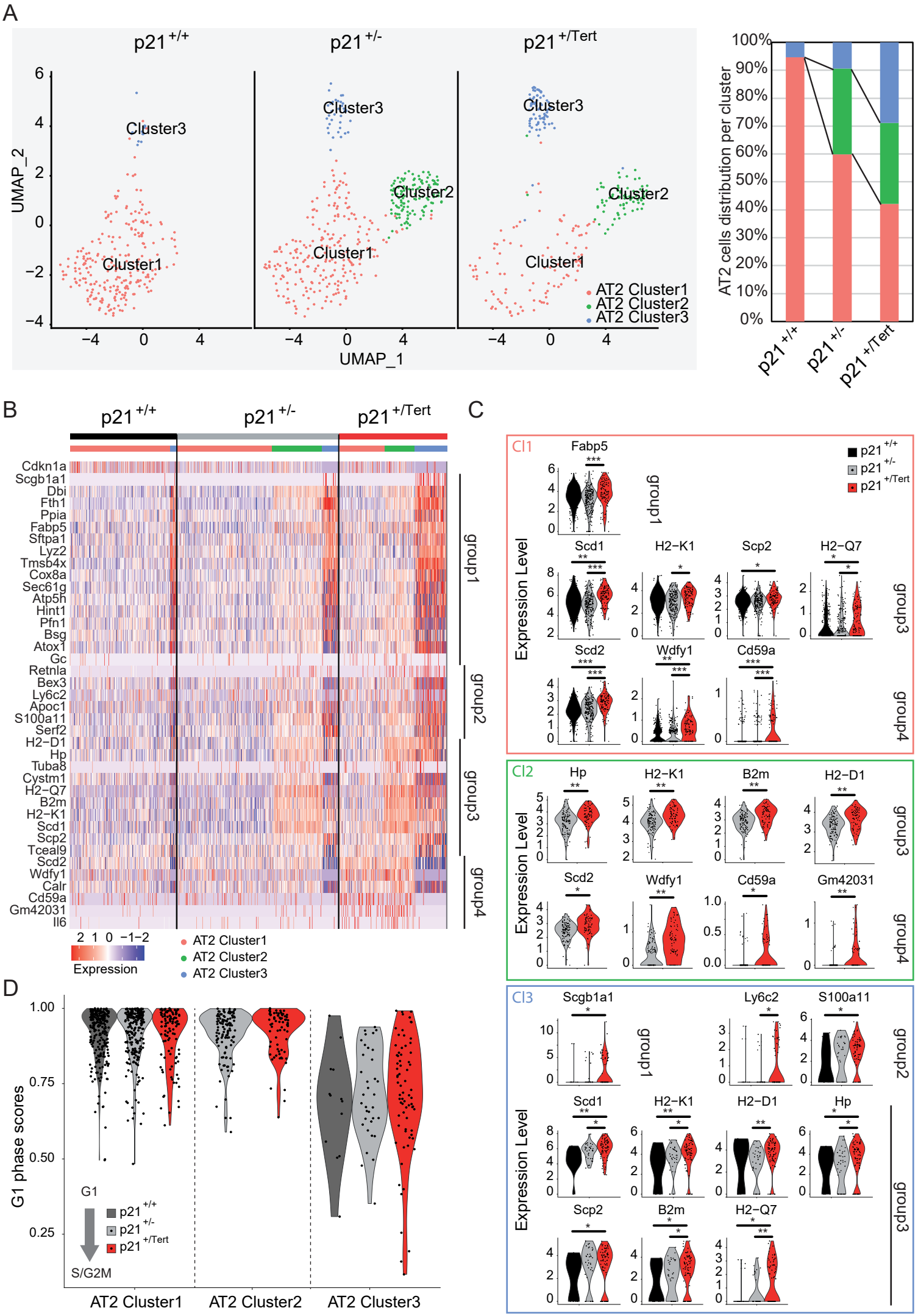
A
p21 +/+
p21 +/-
p21 +/Tert
Cluster3
Cluster2
Cluster1
UMAP_2
UMAP_1
AT2 Cluster1
AT2 Cluster2
AT2 Cluster3
AT2 cells distribution per cluster
B
Cdkn1a
Scgb1a1
Dbi
Fth1
Ppia
Fabp5
Sftpa1
Lyz2
Tmsb4x
Cox8a
Sec61g
Atp5h
Hint1
Pfn1
Bsg
Atox1
Gc
Retnla
Bex3
Ly6c2
Apoc1
S100a11
Serf2
H2−D1
Hp
Tuba8
Cystm1
H2−Q7
B2m
H2−K1
Scd1
Scp2
Tceal9
Scd2
Wdfy1
Calr
Cd59a
Gm42031
Il6
group1
group2
group3
group4
Expression
C
Cl1
Cl2
Cl3
Expression Level
Fabp5
Scd1
H2−K1
Scp2
H2−Q7
Scd2
Wdfy1
Cd59a
Hp
B2m
Gm42031
Scgb1a1
Ly6c2
S100a11
D
G1 phase scores
G1
S/G2M
AT2 Cluster1
AT2 Cluster2
AT2 Cluster3